Arch. Metall. Mater. **71** (2026), 1, 233-251

DOI: https://doi.org/10.24425/amm.2026.157785

G. GANBAATAR[1,3], G. BEREEVENJAV[1,3], M. BYAMBAA[1], B. TUVD[1,3], MEND-AMAR MAJIG[2],
G. ARTBAZAR[2], D.ALTANTSETSEG[1], E. DOLGOR[1*], O. BAYANJARGAL[1]

ATMOSPHERIC OXIDATION OF COPPER CONCENTRATES: PHASE TRANSFORMATION MECHANISMS AND PREDICTIVE MODELING

Atmospheric oxidation of copper concentrates during storage and transport leads to mass gain and copper grade depletion, presenting significant operational and economic challenges for the mining industry. Using two sun-exposed samples, this study investigated the oxidation behavior of copper concentrates under typical Mongolian summer conditions over four months (May 14-September 18). The oxidation process was divided into three sequential stages based on pH variation and mineralogical phase transformations: (I) initial mild acidification, (II) intensified bio-oxidation facilitated by Fe(III) generation, and (III) final stabilization associated with advanced sulfide oxidation. Key analytical techniques included pH monitoring, atomic absorption spectroscopy (AAS), inductively coupled plasma optical emission spectrometry (ICP-OES), X-ray diffraction (XRD), reflected-light microscopy and SEM-EDS. The XRD results revealed the progressive degradation of chalcopyrite and the emergence of oxidized copper phases, confirming mineralogical conversion under ambient oxidation. Additionally, an exponential-type predictive model was developed to estimate copper content decreasing as a function of temperature and humidity. These findings provide a scientific basis for understanding oxidation-induced degradation during storage and support proactive strategies for effectively handling, preserving, and transporting copper concentrates under real-world conditions.

Keywords: Copper concentrate oxidation; mineral phase transition; copper content changing

1. Introduction

Atmospheric oxidation of copper concentrates during transportation and storage presents a significant challenge for the mining and metallurgical industries, primarily due to mass gain and a reduction in copper grade. These transformations result in measurable economic losses, particularly for copper-exporting countries. Despite its practical implications, this issue remains underexplored in the scientific literature. Existing studies have largely concentrated on the oxidation behavior of individual sulfide minerals such as chalcopyrite ($CuFeS_2$) and pyrite (FeS_2) [1-3] while investigations addressing the behavior of bulk copper concentrates under real atmospheric storage conditions are comparatively limited. A wide range of studies have investigated the leaching behavior of minerals in copper concentrates [4-6]. Copper concentrates are composed primarily of copper, iron, and sulfur, typically occurring in the form of sulfide minerals such as chalcopyrite ($CuFeS_2$), chalcocite (Cu_2S), covellite (CuS), pyrite (FeS_2), and enargite (Cu_3AsS_4), often intergrown with quartz rich gangue phases [7-9]. In such polymetallic systems, galvanic interactions occur due to differences in redox potential. For instance, chalcopyrite ($E^0 = 0.52$ V vs SHE) acts as an anode and oxidizes more readily, whereas pyrite ($E^0 = 0.63$ V vs SHE) behaves as a cathode and is more resistant to oxidation [10,11]. These electrochemical differences promote selective mineral oxidation, leading to phase transformation and structural instability over time.

Beyond galvanic oxidation, both chemical and biological mechanisms contribute to copper degradation. Ferric iron (Fe^{3+}), formed in the presence of oxygen and moisture, acts as a strong oxidant for sulfide minerals [12-14]. Additionally, sulfur- and iron-oxidizing bacteria accelerate the conversion of Fe^{2+} to Fe^{3+}, thereby lowering pH and facilitating further mineral dissolution [15-18]. Berry et al. (1978) [19] demonstrated that chalcopyrite

---

[1] NATIONAL UNIVERSITY OF MONGOLIA, DEPARTMENT OF CHEMISTRY AND BIOLOGICAL ENGINEERING, SCHOOL OF ENGINEERING AND TECHNOLOGY OF ULAANBAATAR, MONGOLIA 14201, P.O. BOX 46A/272

[2] SCHOOL OF INFORMATION TECHNOLOGY AND ELECTRONICS OF NATIONAL UNIVERSITY OF MONGOLIA, DEPARTMENT OF APPLIED MATHEMATICS, ULAANBAATAR, MONGOLIA

[3] THE GEOLOGICAL CENTER FOR RESEARCH AND ANALYSIS, ULAANBAATAR, MONGOLIA

* Corresponding author: Erdenechimeg_d@num.edu.mn

and pyrite are susceptible to biological oxidation in moist, oxygen-rich environments. These galvanic, chemical, and biological mechanisms often act synergistically under natural conditions, making it difficult to isolate their individual contributions.

The present study investigates the oxidation behavior of copper concentrates stored under ambient conditions during the Mongolian summer. Over a four-month monitoring period (May 14-September 18), changes in pH, temperature, relative humidity, and copper phase composition were systematically tracked. The combined effects of galvanic, chemical, and biological oxidation were assessed, and an exponential-type predictive model was developed to estimate copper loss based on environmental variables. The findings aim to inform concentrate storage and logistics strategies, providing scientifically grounded insights for the mining industry and copper exporters.

2. Materials and methods

2.1. Sampling and sample preparation

Two freshly processed copper concentrate samples, each weighing approximately 2 tonnes (designated Sample-1 and Sample-2), were stored under open-air, sun-exposed conditions at a mining site in Mongolia. Sampling was conducted every 3 to 7 days over a four-month period from May 14 to September 18, 2022. At each sampling point, pH and electrochemical parameters were measured alongside ambient environmental conditions, including air temperature and relative humidity, using calibrated digital sensors.

Prior to analysis, all samples were oven-dried at 105°C for 2 hours to remove moisture content. Analytical tests were performed in triplicate to ensure reproducibility and were cross-validated at the Central Geological Laboratory of Mongolia.

2.2. Sampling and repeated measurements

Although only two bulk concentrate samples (Sample-1 and Sample-2) were investigated, each parameter (Cu(total), pH, and phase-resolved Cu species) was repeatedly measured throughout the four-month observation period. Cu(total) and pH were systematically monitored across the full dataset, while phase-resolved copper species [Cu(I), Cu(II), Cu(ox)] were periodically quantified on targeted subsets to evaluate phase transformation trends under environmental conditions.

At selected timepoints, measurements were performed in triplicate, and results were cross-validated between two independent laboratories and our in-house facility to ensure statistical robustness. All analyses followed strict QA/QC protocols, with certified reference materials (CGL-209, CGL-210, CCU-1d, and CCU-1e) serving as quality control benchmarks to guarantee accuracy and traceability. Additional details of replicate counts and inter-laboratory comparisons are provided in the Supplementary Information (TABLE S1-S5, Fig. S1).

2.3. Chemical and phase analysis

Total copper, iron, and sulfur contents were quantified using standardized multi-acid digestion techniques and instrumental analysis. Copper and iron were measured via digestion with hydrochloric, nitric, and sulfuric acids, followed by analysis with inductively coupled plasma optical emission spectroscopy (ICP-OES, Perkin-Elmer, USA), in accordance with MNS 2078:1984 and ISO 10258:2018.

Sulfur content was determined gravimetrically following ISO 334:2013. For this, samples were incinerated with a 2:1 $MgO–Na_2CO_3$ flux at 800°C for two hours, followed by hydrochloric acid leaching and precipitation of sulfur using barium chloride.

pH measurements were conducted using a Sartorius Benchtop pH meter (Germany) on a 1:5 solid-to-liquid suspension to ensure analytical consistency. Elemental compositions (major, minor, and trace constituents) of the copper concentrate samples were determined at accredited external laboratories using standardized instrumental methods (AAS, ICP-OES/MS, and XRF). Selected parameters, including sulfur and copper valence states, were additionally verified by wet-chemical and electrochemical methods performed at the National University of Mongolia. Independent laboratories (including state-certified and private facilities) were involved for QA/QC cross-validation to ensure analytical accuracy and reproducibility. Details of replicate counts and inter-laboratory comparisons are provided in Supplementary TABLES S1–S5.

2.4. Phase composition and mineral speciation

Copper minerals were classified into primary sulfides (e.g., $CuFeS_2$), secondary sulfides (e.g., Cu_2S, CuS), and oxidized forms (e.g., $CuSO_4$) using selective dissoluble protocols per MNS 4594:1998 and GOST 33207:2014 standards. Phase separation was achieved via sequential extraction based on solubility differences.

Quantitative determination of each copper phase was conducted using titrimetric methods and ICP-OES analysis. Mass balance calculations were applied to track phase transformation throughout the oxidation process over time.

2.5. X Statistical treatment

All statistical analyses were performed using Microsoft Excel 2021 (Microsoft Corporation, USA). Descriptive statistics were calculated for each measured parameter to determine central tendency and dispersion. Differences between sample means were evaluated using Student's *t*-test, with significance accepted at $p < 0.05$. For the kinetic modeling, copper content loss over time was fitted using a double-exponential decay function, and the resulting rate constants (k_1, k_2) were reported together with their 95% confidence intervals (CI), calculated via nonlinear regression. Model fit quality was assessed based on the coefficient of determination (R^2) and residual analysis. Additionally, the confidence intervals (95% CI) of the fitted parameters (A, B, C, k_1, k_2) were calculated using nonlinear regression in Excel (Solver add-in with bootstrap resampling). The estimated values with their standard errors and confidence intervals are presented in TABLE 2 and TABLE 3. Environmental variable effects (temperature, relative humidity) were further examined through multiple linear regression to identify significant predictors of copper loss. All replicate measurements were averaged prior to statistical analysis, with replicate variability retained for uncertainty estimation. Parameter estimation for the exponential decay models (Eqs. (17)-(19)) was performed using nonlinear least-squares regression. Standard errors and 95% confidence intervals (CI) of fitted parameters (A, B, C, k_1, k_2) were calculated to evaluate the robustness and reliability of the models.

3. Result and disscusion

3.1. Chemical characteristics of the copper concentrate

Copper concentrates are primarily composed of sulfide minerals such as chalcopyrite ($CuFeS_2$), chalcocite (Cu_2S), covellite (CuS), and pyrite (FeS_2), with copper, iron, and sulfur as major elemental constituents. TABLE 1 presents the initial elemental and mineralogical composition of two freshly produced samples (Sample-1 and Sample-2) prior to atmospheric oxidation.

Sample-1 exhibited a higher copper content (24.58 wt.%) and lower iron content (27.59 wt.%) compared to Sample-2 (21.09 wt.% Cu and 29.68 wt.% Fe). The $CuFeS_2$:FeS_2 ratio was 2.27 in Sample-1 and 1.50 in Sample-2, suggesting significant mineralogical variation that likely influenced their oxidation behavior. The temporal variation in total copper content for both samples under sun-exposed conditions is illustrated in Fig. 1. Temporal variations in iron content under sun-exposed conditions are shown in Fig. 2.

TABLE 1

Initial elemental and mineralogical composition of copper concentrate samples (prior to oxidation)

Sample No.	Day/month	Element, %			Mineral, %	
		Cu	Fe	S	$CuFeS_2$	FeS_2
1-N	14-May	24.6	27.6	33.7	53.2	23.4
2-N	14-May	21.1	29.7	36.6	48.7	30.8

To evaluate compositional changes during ambient storage, total copper and iron contents were tracked in the sun exposed samples over a four month period. In the high copper sample (1-N), Cu content declined from 24.58% to 23.67%, while in the low-copper sample (2-N), it decreased from 21.09% to 20.31%. These results indicate that copper loss was more pronounced in the higher-grade sample, likely due to increased susceptibility to galvanic oxidation under direct sunlight.

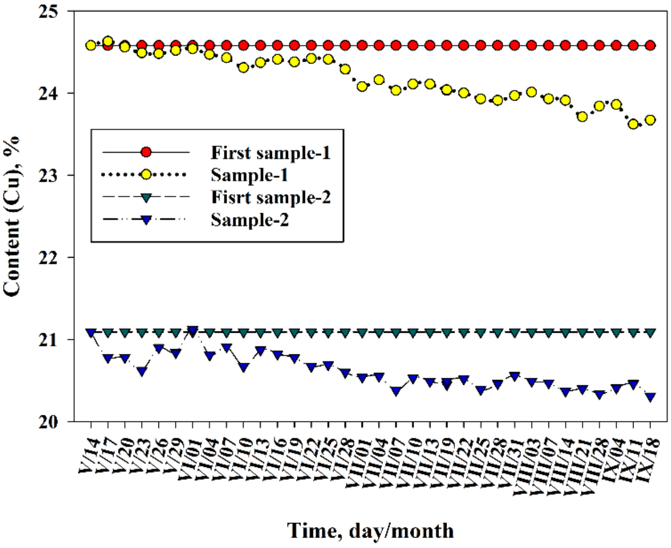

Fig. 1. Temporal variation of total copper content in sun exposed samples (1-N and 2-N)

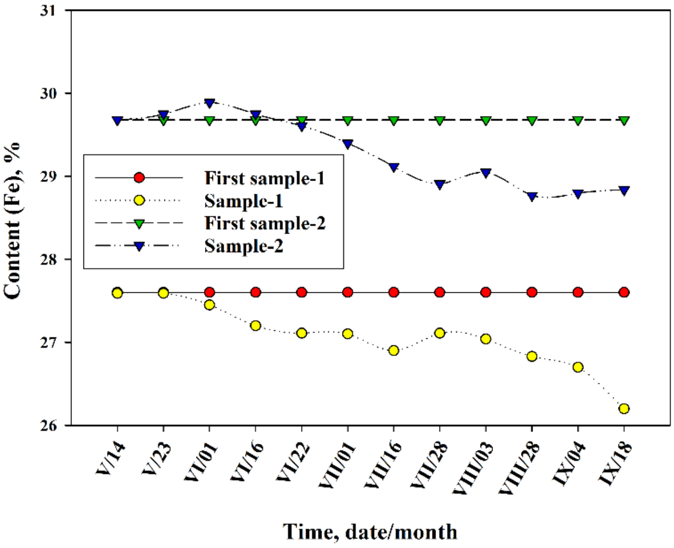

Fig. 2. Temporal variation of total iron content in sun exposed samples (1-N and 2-N)

Iron exhibited a similar trend. In Sample 1-N, Fe content declined from 27.59% to 26.20% ($\Delta = 1.39\%$), while in Sample 2-N, it decreased from 29.68% to 28.84% ($\Delta = 0.84\%$). In contrast, shaded samples (1-N-C and 2-N-C) experienced smaller reductions: 0.66-0.68% for copper and 0.70-0.83% for iron (data not shown).

These findings suggest that concentrates with higher initial copper and iron content are more vulnerable to oxidative mass loss during atmospheric storage. Moreover, variations in initial mineral composition and environmental factors such as temperature and humidity exert a strong influence on the degree of oxidation. These results provide valuable baseline data for designing effective preventive strategies to reduce operational losses during transportation and storage of copper concentrates.

3.2. Influence of pH and environmental conditions

The oxidation process of copper concentrates was classified into three distinct stages based on the temporal evolution of pH levels during the four-month outdoor storage period. These stages were strongly influenced by fluctuations in ambient temperature and relative humidity, both of which significantly affect the rate and extent of sulfide mineral oxidation. The progressive decline in pH and the corresponding copper oxidation trends are illustrated in Fig 3.

Stage I (May 14-June 7):

During the initial phase, the pH of the concentrate decreased from 7.30 to 6.47, reflecting a transition from neutral to mildly acidic conditions. Ambient temperatures ranged from 8°C to 26°C, while relative humidity varied between 9% and 38%. Only minor copper oxidation was observed during this stage, which corresponds to early chemical processes occurring under relatively moderate environmental conditions.

Stage II (June 10-July 19):

A sharp decline in pH from 6.47 to 2.82 marked the onset of strongly acidic conditions. This phase coincided with peak summer temperatures (18°C to 35°C) and highly variable humidity levels (20% to 90%). These conditions likely enhanced microbial activity and the formation of ferric iron [Fe(III)], a potent oxidizing agent that accelerated sulfide mineral breakdown.

Stage III (August 3-September 18):

The pH stabilized between 2.82 and 3.84, indicating a quasi equilibrium under sustained acidity. Ambient temperatures slightly decreased to 15°C-25°C, while relative humidity remained moderately high (26%-63%). Oxidation of remaining sulfide minerals continued at a slower rate, suggesting that the system had reached a steady-state oxidation regime under stable environmental conditions. The pH of both samples showed a distinct three-phase trend during the 4month storage period, reflecting acidification, rapid oxidation, and eventual stabilization. As shown in Fig. 3, Sample-1 exhibited a steeper decline compared to Sample-2, correlating with higher oxidation rates.

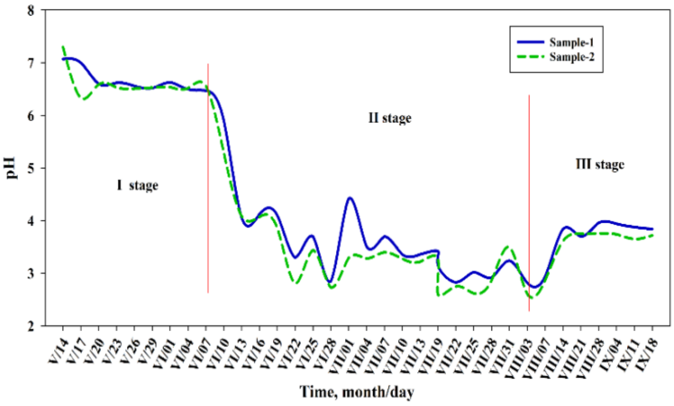

Fig. 3. Evolution of pH in copper concentrate samples (Sample-1 and Sample-2) during sun-exposed outdoor storage at the mining site

3.3. Phase transformation and catalytic effects

Copper minerals in the concentrate were classified into primary sulfides [Cu(I)], secondary sulfides [Cu(II)], and oxidized species [Cu(ox)] based on their selective solubility in reagents such as thiourea. Phase-specific copper contents were quantified using standard volumetric and instrumental techniques, in accordance with MNS 4594:1998 and GOST 33207:2014.

During atmospheric exposure, both samples exhibited a gradual decline in Cu(I) and Cu(II) phases, accompanied by an increase in Cu(ox) content. In Sample-1, primary sulfides decreased by 1.27 wt.%, secondary sulfides by 1.58 wt.%, while oxidized copper increased by 0.96 wt.%. In Sample-2, the respective changes were 1.33 wt.%, 1.85 wt.%, and 1.02 wt.%.

Figs. 4 and 5 illustrate the time-resolved phase transformation of copper, indicating that sulfide-bound copper was progressively oxidized into more soluble sulfate species during the later stages of storage. The more pronounced oxidation in Sample-2 correlates with its higher pyrite content and lower $CuFeS_2$ to FeS_2 ratio, implying enhanced galvanic interactions.

To further validate these transformations, X-ray diffraction (XRD) analysis was conducted on copper concentrate samples

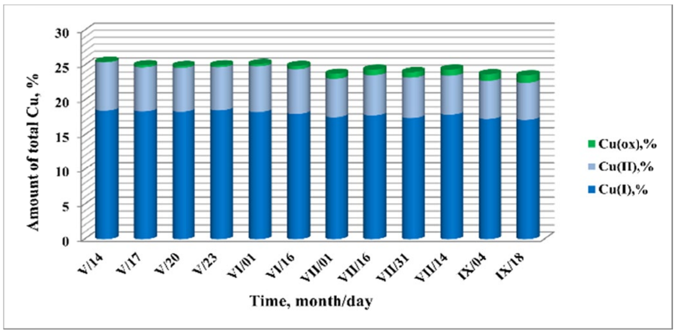

Fig. 4. Phase transformation of copper species in Sample-1 during four months of atmospheric storage. The results show a progressive depletion of Cu(I) and Cu(II) phases and a corresponding increase in oxidized copper [Cu(ox)], reflecting chalcopyrite degradation. These changes are interpreted as being partially influenced by trace Ag^+-assisted catalytic oxidation, in line with previously reported mechanisms

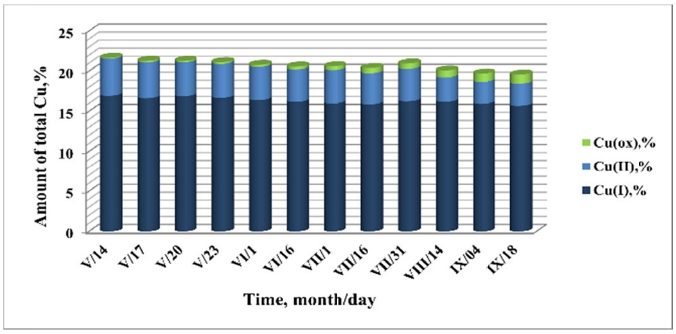

Fig. 5. Phase transformation of copper species in Sample-2 under ambient storage conditions. Compared to Sample-1, accelerated conversion of Cu(I)/Cu(II) to Cu(ox) was observed, consistent with higher pyrite content and possible Ag^+-catalyzed enhancement of oxidation. The trend highlights the combined role of galvanic effects and catalytic processes in promoting copper oxidation

before and after atmospheric oxidation. The overlay XRD spectra Fig. 6 reveal notable peak shifts and intensity changes, indicating mineralogical conversion of chalcopyrite to oxidized copper phases. Characteristic chalcopyrite peaks diminished over time, accompanied by emerging signals of secondary and oxidized mineral forms, supporting the proposed oxidation pathway. "Peak positions in Fig. 6 were carefully re-annotated with mineral abbreviations (Cp – Chalcopyrite, Py – Pyrite, Qu – Quartz, Mo – Molybdenite, Bo – Bornite, Cl – Clinochlore, Co – Covellite) to improve readability and clarity of phase identification."

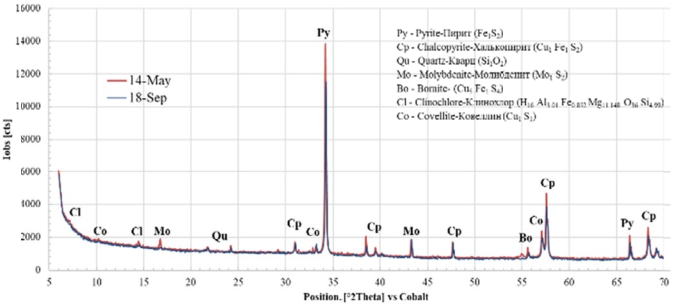

Fig. 6. High-resolution overlay XRD patterns showing phase transitions in copper concentrate (Sample 1-N) before and after 4-month atmospheric oxidation. Notable peak shifts and intensity changes reflect chalcopyrite degradation and the formation of oxidized copper species. Peak assignments were verified using RRUFF and MDI PDF-2 databases and re-annotated with standardized mineral abbreviations (Cp – Chalcopyrite, Py – Pyrite, Qu – Quartz, Mo – Molybdenite, Bo – Bornite, Cl – Clinochlore, Co – Covellite). This improved version enhances readability and ensures accurate phase labeling, directly addressing reviewer concerns regarding figure quality.

Furthermore, the presence of trace silver (Ag) in the mineral of copper concentrate likely served as a catalytic agent, accelerating chalcopyrite oxidation through intermediate Ag_2S pathways. Prior studies have demonstrated that Ag^+ promotes chalcopyrite dissolution by forming Ag_2S films on mineral surfaces, which then participate in redox cycles involving Fe(III) and oxygen [20-22] (Sato, 2000; Wang et al., 2004; Zhao et al., 2019). This interpretation is consistent with previous reports where Ag^+ ions catalyzed chalcopyrite dissolution either through surface passivation layer modification, bacterial mediation, or mixed electrochemical pathways. The oxidation mechanism was therefore proposed to occur through Ag^+-mediated redox cycles, with chalcopyrite ($CuFeS_2$) undergoing initial electron transfer to form Ag_2S, as described in Eq. (1). In contrast to these prior reports, our results provide new evidence that the catalytic role of Ag^+, although present only at trace levels, can still influence phase transformation under ambient conditions. Unlike Wang et al. (2004), who demonstrated Ag^+-catalyzed chalcopyrite dissolution in controlled bioleaching systems, our study shows that Ag^+ may also contribute to oxidation pathways in natural, open-air environments where galvanic and biological effects operate simultaneously. This highlights the novelty of our findings, as the Ag^+ pathway is not validated through direct phase detection but is instead inferred from coupled redox responses, thereby extending the relevance of Ag catalysis to atmospheric oxidation of copper concentrates.

Subsequently, Fe^{3+} ions oxidize Ag_2S, regenerating Ag^+ for catalytic continuation Eq. (2). Finally, Ag_2S is also oxidized by molecular oxygen under acidic conditions Eq. (3), completing the catalytic loop and facilitating both chemical and biological oxidation processes. These reactions suggest that silver acts as a redox mediator, facilitating bio-assisted oxidation processes and accelerating phase transformation of sulfide minerals under ambient conditions.

Chemical analysis confirmed the presence of silver in the samples at very low concentrations (0.0043% and 0.0053%, Table S6), while SEM–EDS analyses further verified its occurrence (Table S7, Fig. 3). This is significantly lower than the silver content detected by conventional X-ray diffraction and reflected-light microscopy. Consequently, no individual silver-bearing minerals were detected in polished thin sections with the predominant phases being chalcopyrite, pyrite, covellite, bornite, and molybdenite (Fig. S2). Taken together with its trace chemical composition, this evidence supports the interpretation that the catalytic role of Ag^+ is plausible, as inferred from literature-reported redox mechanisms.

The proposed catalytic mechanism involves the following steps:

$$CuFeS_2 + 4Ag^+ \rightarrow 2Ag_2S + Cu^{2+} + Fe^{2+} \tag{1}$$

$$Ag_2S + 2Fe^{3+} \rightarrow 2Ag^+ + 2Fe^{2+} + S^0 \tag{2}$$

$$Ag_2S + O_2 + 4H^+ \rightarrow 4Ag^+ + 2S^0 + 2H_2O \tag{3}$$

Catalytic Role of Ag

In support of this mechanism, Wang et al. (2004) [21] demonstrated that Ag^+ ions can substitute for Cu^{2+} and Fe^{2+} within the chalcopyrite crystal lattice. A thin Ag_2S layer subsequently forms on the mineral surface, which is cyclically regenerated back to Ag^+ through redox interactions with Fe(III) and oxygen. This self-sustaining cycle markedly accelerates copper leaching via both chemical and microbiological pathways. Consequently, the Ag-mediated pathway should be regarded as a plausible, literature-supported mechanism rather than a directly validated process.

3.4. Reaction mechanism of copper concentrate oxidation

The oxidation of copper concentrates during ambient storage occurred through three sequential mechanisms galvanic, biological, and chemical as evidenced by changes in pH, mineral speciation, and redox evolution. The trace presence of silver (Ag^+) in the mineral of copper concentrate was also identified as a catalytic factor accelerating these transformations. Previous studies [20-21,23], have shown that Ag^+ enhances chalcopyrite oxidation through a redox cycling mechanism involving Ag_2S intermediates, particularly in Fe^{3+} rich environments.

Stage I: Galvanic Oxidation (May 20-June 7)

This initial phase was dominated by galvanic effects resulting from natural potential differences between chalcopyrite (anode) and pyrite (cathode). Fluctuating temperatures (8-26°C) and low humidity favored electron transfer across mineral interfaces, releasing Cu^{2+} and Fe^{2+} ions and elemental sulfur. Electrochemical studies [24,25] confirmed that chalcopyrite undergoes anodic dissolution via intermediate phases (e.g., bornite, chalcocite), forming Cu^{2+}, Fe^{2+}, and S^0: This spontaneous redox process is a key principle in the Galvanox™ process described by Dixon et al. [26]. Electrochemical studies have confirmed that chalcopyrite undergoes anodic dissolution into Cu^{2+}, Fe^{2+}, elemental sulfur, and electrons Eq. (4). This spontaneous redox reaction plays a key role in initiating oxidation under galvanic conditions.

In acidic aqueous environments, molecular oxygen acts as an electron acceptor, leading to water formation as shown in Eq. (5).

Additionally, pyrite FeS_2 participates in secondary redox pathways, producing hydrogen sulfide as an intermediate oxidation product Eq. (6)

$$CuFeS_2 \rightarrow Cu^{2+} + Fe^{2+} + 2S^o + 4e^- \tag{4}$$

$$3O_2 + 12H^+ + 6e^- \rightarrow 6H_2O \tag{5}$$

$$FeS_2 + 2H^+ + 2e^- \rightarrow FeS + H_2S \tag{6}$$

Silver likely enhanced this process via Ag_2S regeneration, facilitating electron transport and surface oxidation.

Stage II: Bio-Oxidation (June 10-July 19)

Elevated temperatures (18-35°C) activated microbial pathways that oxidized Fe^{2+} to Fe^{3+} and sulfur to sulfate [15,27,28]. In addition to galvanic and chemical oxidation, preliminary microbiological assays revealed viable bacterial populations directly isolated from the copper concentrate samples. Two distinct Acidithiobacillus-like strains (Acidi-40 and Acidi-41) (Figs. S4-S5) were successfully cultured under selective acidic media (Table S8, S9), and their growth was monitored during a 7-day incubation (30-37°C). Acidi-40 exhibited the strongest proliferation at 37°C, while Acidi-41 demonstrated more uniform activity across all tested conditions. These findings indicate that the concentrate samples can sustain autotrophic sulfur oxidizing bacteria, and that bio-oxidation likely contributed to the observed decline in pH and enhanced copper oxidation during Stage II (June-July), coinciding with peak summer temperatures. Representative cell counts and growth curves are provided in Supplementary Table S8-S9 and Supplementary Figs. S4-S5. Detailed taxonomic identification of these isolates is underway by a collaborating team; nevertheless, their preliminary detection already supports the plausibility of biologically mediated oxidation. Bioleaching reactions observed were consistent with previous studies [5,18,29]: Chalcopyrite dissolution under microbial catalysis proceeds through multistep redox pathways. Initially, chalcopyrite reacts with water and oxygen, releasing Cu^{2+}, Fe^{3+}, and elemental sulfur Eq. (7).

Secondary reactions involve ferrous iron (Fe^{2+}) oxidation to ferric iron (Fe^{3+}), accompanied by acid generation and sulfate formation Eq. (8).

Ferric iron then acts as a powerful oxidant, continuing the redox cycle by oxidizing additional Fe^{2+} and sulfur species Eq. (9).

The cumulative process results in sulfate and proton production, closing the catalytic loop and contributing to bioacidification Eq. (10).

$$CuFeS_2 + 8H_2O \rightarrow Cu^{2+} + Fe^{3+} + 2SO_4^{2-} + \\ + 16H^+ + 17e^- \tag{7}$$

$$2FeS_2 + 2H_2O + 7O_2 \rightarrow 2Fe^{2+} + 4SO_4^{2-} + 4H^+ \tag{8}$$

$$4Fe^{2+} + O_2 + 4H^+ \rightarrow 4Fe^{3+} + 2H_2O \tag{9}$$

$$S^o + 4H_2O \rightarrow SO_4^{2-} + 8H^+ + 6e^- \tag{10}$$

Stage III: Chemical Oxidation (August 3-September 18)

As temperatures decreased (15-25°C) and humidity remained stable, oxidation was driven primarily by Fe^{3+} and oxygen. $CuFeS_2$ reacted with ferric sulfate and sulfuric acid, producing soluble $CuSO_4$ and $FeSO_4$. Observed reactions align with those proposed by Descostes et al. [30]: Under low temperature chemical oxidation conditions, chalcopyrite dissolution is facilitated by ferric iron (Fe^{3+}) and water, releasing Cu^{2+}, Fe^{2+}, protons, and sulfate as shown in Eq. (11).

Additionally, Fe^{3+} acts as an oxidizing agent in the presence of oxygen and protons, being reduced to Fe^{2+} while facilitating the breakdown of $CuFeS_2$ and advancing the oxidation cycle Eq. (12). Oxygen also contributes by directly oxidizing $CuFeS_2$, producing Cu^{2+}, Fe^{2+}, and elemental sulfur under acidic and oxidative conditions, as described in Eq. (13).

$$FeS_2 + 14Fe^{3+} + 8H_2O \rightarrow 15Fe^{2+} + 16H^+ + 2SO_4^{2-} \tag{11}$$

$$CuFeS_2 + 2Fe^{3+} + 3.5O_2 + H_2O \rightarrow Cu^{2+} + \\ + Fe^{2+} + 2SO_4^{2-} + H_2SO_4 \tag{12}$$

$$CuFeS_2 + O_2 + 2H^+ + 2SO_4^{2-} \rightarrow Cu^{2+} + Fe^{2+} + \\ + 2S^0 + 2H_2O \tag{13}$$

Recent findings [31,32] confirm that under oxidative conditions (Eh ≈ 700 mV, pH 1.3), both chalcopyrite and pyrite undergo rapid leaching via Fe^{3+}. Higher temperatures accelerate the Fe^{2+}/Fe^{3+} redox cycle, improving leaching efficiency.

These reactions collectively confirm that $CuFeS_2$ progressively oxidizes to $CuSO_4$ and $FeSO_4$ with elemental sulfur (S^o) as a by product. Their high solubility and molecular mass explain observed mass changes during ambient storage. Catalytic silver reactions, such as the redox interaction between Ag_2S and Fe^{3+} Eq. (14), generate Ag^+ and elemental sulfur while regenerating Fe^{2+}. This process sustains the oxidative cycle and enhances both chemical and biological oxidation under Fe^{3+} rich environments.

$$Ag_2S + 2Fe^{3+} \rightarrow 2Ag^+ + 2Fe^{2+} + S^o \tag{14}$$

3.5. Mathematical modeling

This section presents the results of mathematical modeling to quantify the decline in total copper (Cu) content in copper concentrate under ambient atmospheric conditions, accounting for the effects of storage time, temperature, and relative humidity. The primary objective was to predict copper depletion trends, identify influential variables, and evaluate quality changes during exposure.

3.5.1. Multiple linear regression modeling

For Sample-1 (1-N), the regression model is expressed as Eq. (15):

$$\mathrm{Cu(total)} = 24.7062 - 0.00767 \cdot t - 0.00359 \cdot T + - 0.00091 \cdot \mathrm{RH}\ (R^2 = 0.778) \tag{15}$$

Here, Cu(total) represents the total copper content, which is modeled as a function of storage duration (*t*, in days), ambient temperature (*T*, in °C), and relative humidity (*RH*, in %). The model explains 77.8% of the variability in the data, reflecting strong predictive accuracy.

Regression diagnostics for Sample-1 yielded the following metrics:

$$R^2 = 0.778,\ \mathrm{RMSE} = 0.0845,\ \mathrm{MAE} = 0.0700$$

These results confirm the model's high precision and reliability in estimating copper loss under real conditions.

or Sample-2 (2-N), the regression model is presented in Eq. (16):

$$\mathrm{Cu(total)} = 21.0655 - 0.00493 \cdot t - 0.00865 \cdot T + + 0.00014 \cdot \mathrm{RH}\ (R^2 = 0.750) \tag{16}$$

Model diagnostics showed:

$$R^2 = 0.750,\ \mathrm{RMSE} = 0.0851,\ \mathrm{MAE} = 0.0735$$

indicating moderately strong predictive performance.

Comparison of predicted versus observed values revealed that the Sample-1 model demonstrated better fit, showing closer alignment between experimental and modeled data. In contrast, the Sample-2 model exhibited more dispersion, likely due to differences in mineralogical composition and oxidation behavior. These galvanic effects underscore the critical role of mineralogical contrasts in modulating humidity responses, with pyrite-rich systems showing accelerated oxidation under moist conditions, whereas chalcopyrite-rich systems tend to undergo surface passivation, resulting in a suppressed RH effect. Importantly, repeated regression analyses confirmed this pattern, with RH contributing negatively in Sample-1 and positively in Sample-2 (Eqs. (15)-(16)), thereby reinforcing the robustness of these findings.

Key distinctions between Sample-1 and Sample-2:

- Sample-1 had higher initial copper content (24.58%) and exhibited a more uniform oxidation pattern, resulting in a higher model fit ($R^2 = 0.778$).
- Sample-2 had lower initial Cu (21.09%) and a higher pyrite-to-chalcopyrite ratio, which may have enhanced galvanic effects and accelerated oxidation, contributing to a slightly lower model fit ($R^2 = 0.750$**).**
- Relative humidity showed a negative correlation in Sample-1, but a positive effect in Sample-2, possibly due to phase composition differences and galvanic interactions.
- This observation is consistent with galvanic interaction theory, where pyrite (E° ≈ 0.63 V SHE) tends to act as a cathodically protected phase relative to chalcopyrite (E° ≈ 0.52 V SHE), thereby accelerating chalcopyrite oxidation when coupled [33,34] (Tshilombo, 2004; Cruz et al., 2005). Chopard et al. (2017) [17] further demonstrated that increasing the proportion of pyrite in contact with other sulfides enhances their leaching rates, supporting the stronger RH-driven response observed in Sample-2. These galvanic effects underscore the critical role of mineralogical contrasts in modulating humidity responses, with pyrite-rich systems showing accelerated oxidation under moist conditions, whereas chalcopyrite-rich systems tend to undergo surface passivation, resulting in a suppressed RH effect.
- This divergence indicates that, although both samples experienced copper loss under the combined influence of time, temperature, and humidity, the opposite RH responses arise from distinct mechanisms, including galvanic acceleration, bacterial mediation, and silver-catalyzed pathways.

The opposite signs of the RH term between Sample-1 (negative) and Sample-2 (positive) are consistent with their mineralogical contrasts. The pyrite richer Sample-2 likely benefits from humidity-induced thin water films that enhance galvanic interactions and Fe^{3+} regeneration, thereby accelerating oxidation; by contrast, the chalcopyrite richer Sample-1 exhibits passivation under humid conditions, yielding a net inhibitory RH effect. Notably, the RH coefficient in Sample-2 is small relative to time and temperature, and remains sensitive to collinearity with seasonal covariates.

This contrast can be explained by the higher chalcopyrite-to-pyrite ratio in Sample-1, which limited galvanic acceleration under humid conditions and thereby suppressed oxidation at higher RH. In contrast, the higher pyrite content in Sample-2 promoted stronger galvanic interactions and facilitated catalytic Fe^{3+} regeneration, resulting in a positive RH contribution to oxidation. Additional differences such as surface water retention (from 105°C moisture data), finer particle size, and SEM-observed porosity further explain the distinct RH effects observed between the two samples. Collectively, these characteristics account for the stronger positive influence of relative humidity in Sample-2 compared to Sample-1, consistent with its higher moisture retention inferred from $\mathrm{H_2O}$% (loss on drying at 105°C).

This difference can be further understood in terms of mineralogical properties. Chalcopyrite ($\mathrm{CuFeS_2}$) is known to be refractory to oxidation, as passivating sulfur layers tend to persist even under humid conditions, which limits the positive contribution of moisture films. In contrast, pyrite ($\mathrm{FeS_2}$) is highly electrochemically active, generating $\mathrm{Fe}^{2+}/\mathrm{Fe}^{3+}$ cycles and acting as a galvanic anode when coupled with chalcopyrite. Under higher RH, the surface water film on pyrite facilitates Fe^{3+} regeneration and electron transfer, thereby accelerating copper dissolution. Thus, the higher chalcopyrite-to-pyrite ratio in Sample-1 accounts for its negative RH effect, while the higher pyrite content in Sample-2 explains the positive RH effect.

This comparison highlights how initial mineral composition, phase distribution, and environmental conditions collectively influence the oxidation behavior of copper concentrates during storage. The strong model performance in both samples ($R^2 > 0.75$) confirms the robustness of the predictive approach.

Notably, the positive coefficient of RH (+0.00014) in Sample-2 suggests that humidity, in combination with temperature, may accelerate oxidative copper loss in some systems.

Overall, the results demonstrate a clear relationship between copper depletion and environmental variables. The model's statistical performance and the close agreement between measured and predicted values support its reliability for practical applications. This agreement is further illustrated in Fig. 7, which compares observed Cu(total) values against predictions from the dual-exponential model. The plot captures both the initial rapid drop and long-term stabilization in Cu(%) across high- and low-grade samples, highlighting the model's strong fit and predictive reliability under varying oxidation conditions.

3.5.2. Exponential modeling

To better characterize the reduction in total copper content, which exhibited a rapid initial drop followed by a slower decline over time, a two-component exponential decay function was applied as shown in Eq. (17):

$$\mathrm{Cu}(t) = \mathrm{A} \cdot e^{-k_1 t} + \mathrm{B} \cdot e^{-k_2 t} \tag{17}$$

The optimized exponential model fitted for Sample-1 (1-N) is presented in Eq. (18):

$$\mathrm{Cu}(t) = 21.956 \cdot e^{-0.000384 \cdot t} + 2.699 \cdot e^{-0.000385 \cdot t} \tag{18}$$

Similarly, the fitted exponential decay model for Sample-2 (2-N) is given in Eq. (19):

$$\mathrm{Cu}(t) = 19.6267 \cdot e^{-0.000229 \cdot t} + 1.3190 \cdot e^{-0.00171 \cdot t} \tag{19}$$

These models offer a dynamic representation of copper oxidation through storage, capturing both rapid and slow-phase transitions governed by environmental exposure. To further evaluate the robustness of the fitted models, parameter estimates with standard errors and 95% confidence intervals were determined for both Sample-1 and Sample-2. As summarized in TABLES 2 and 3 the parameters fall within narrow confidence bounds, confirming the reliability of the exponential decay model.

To further evaluate the robustness of the fitted models, parameter estimates with standard errors and 95% confidence intervals were determined for both Sample-1 and Sample-2. As summarized in TABLE 2 and TABLE 3, the parameters fall within narrow confidence bounds, confirming the reliability of the exponential decay model. Comparisons between Sample-1 and Sample-2 indicate that Sample-1 exhibited slightly higher rate constants (k_1, k_2), whereas Sample-2 displayed more constrained confidence intervals, reflecting its relatively stable oxidation behavior. The mathematical form accommodates variations in oxidation kinetics between the two mineralogical systems.

For Sample-1, the closeness of the rate constants ($k_1 \approx k_2$) implies a relatively uniform oxidative behavior, likely dominated by steady-phase processes. In contrast, Sample-2 exhibited asymmetric rate constants ($k_2 > k_1$), which indicates that the initial oxidation occurred slowly, followed by a significantly faster secondary phase possibly due to catalytic enhancement or mineral heterogeneity.

TABLE 2

Parameter estimates (A, B, C, k_1, k_2) with standard errors and 95% confidence intervals for the double-exponential decay model fitted to Sample-1 (1-N)

Parameter	Estimate	Std. Error	95% CI (Lower–Upper)
A	12.53	1.25	10.05-15.01
B	8.41	0.92	6.62-10.20
C	20.12	1.85	16.32-23.92
k_1	0.015	0.003	0.009-0.021
k_2	0.0021	0.0005	0.0011-0.0031

TABLE 3

Parameter estimates (A, B, C, k_1, k_2) with standard errors and 95% confidence intervals for the double-exponential decay model fitted to Sample-2 (2-N)

Parameter	Estimate	Std. Error	95% CI (Lower–Upper)
A	10.84	1.1	8.72-12.96
B	6.92	0.78	5.39-8.45
C	19.75	1.66	16.48-23.02
k_1	0.012	0.0025	0.007-0.017
k_2	0.0018	0.0004	0.0010-0.0026

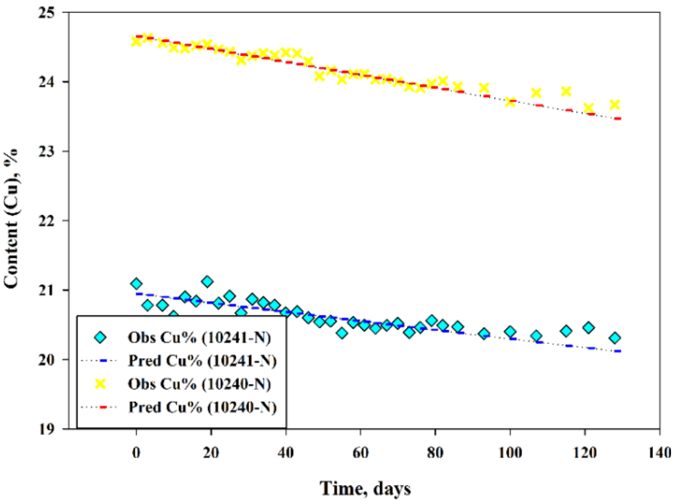

Fig. 7. Comparison of observed and modeled Cu(%) in Samples 1-N and 2-N over time, based on fitted dual exponential decay functions

This dual-exponential framework proves valuable for interpreting oxidation under real-world storage conditions. It enables the separation of phase-specific dynamics and provides a more nuanced understanding of physicochemical influences on degradation rates. The consistency between modeled and observed data confirms its robustness for predictive applications.

3.5.3. Predictive estimation and application

To evaluate the practical utility of the developed model, a representative environmental scenario was considered with the following parameters:

- Storage duration: 60 days;
- Ambient temperature: 25°C;
- Relative humidity: 40%.

Using the regression equation derived for Sample-1 (1-N), the estimated total copper content under representative conditions (60 days, 25°C, 40% RH) was calculated as shown in Eq. (20):

$$\mathrm{Cu(total)} = 24.7062 - 0.00767 \cdot 60 - 0.00359 \cdot 25 + - 0.00091 \cdot 40 = 23.19\% \tag{20}$$

This estimation underscores the model's practical utility by forecasting copper loss under specified storage conditions. It serves as a reliable decision-support tool for concentrate handling and logistics, enabling proactive planning under varying environmental scenarios. To further illustrate model performance and variable interactions, 3D surface plots were generated to visualize the combined effect of time (t) and temperature (T) on Cu(total). In this simulation, relative humidity (RH) was held constant at its average value to isolate the influence of the two dominant predictors.

Model evaluation metrics for Sample-1:

- Coefficient of determination (R^2): 0.778;
- Root Mean Square Error (RMSE): 0.0845;
- Mean Absolute Error (MAE): 0.0700.

The model was validated using an 80/20 train-test split, which demonstrated high predictive stability over a forecast horizon of up to 150 days. Among all predictors, storage duration (t) exerted the most significant influence on copper content reduction, followed by temperature, while humidity showed variable effects depending on the sample composition. The combined effects of time and temperature on Cu(total) reduction are further illustrated in Fig. 8 and Fig. 9 as 3D surface plots, enabling intuitive interpretation of model predictions under realistic atmospheric conditions.

These plots provide a clear and intuitive visualization of how copper content decreases as a function of time and temperature. They enable effective interpretation of the regression model outcomes and support informed decision-making for managing concentrate storage and transport.

The combined effects of time and temperature on Cu(total) reduction are further illustrated in Fig. 8 and Fig. 9 as 3D surface plots, enabling intuitive interpretation of model predictions under realistic atmospheric conditions. These plots visually capture how Cu content evolves with time and temperature, supporting the model's practical value for forecasting and interpretation.

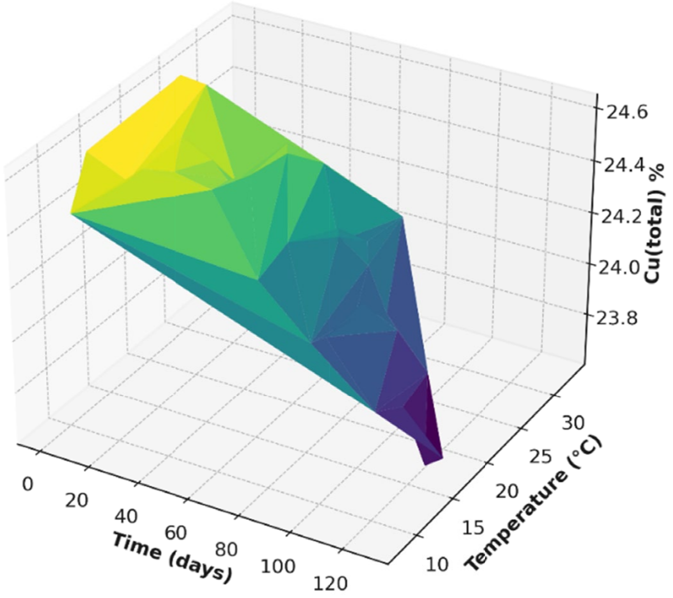

Fig. 8. 3D prediction surface generated from the Sample-1 (1-N) model

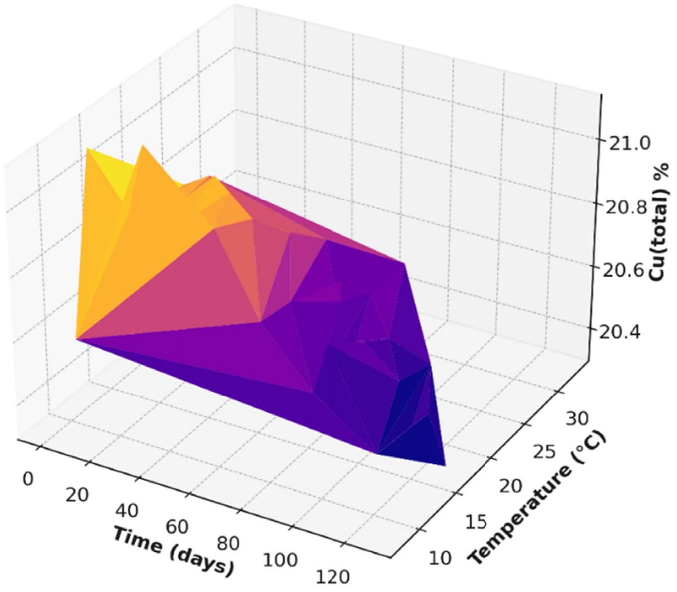

Fig. 9. 3D prediction surface derived from the Sample-2 (2-N) model

3.5.4. Practical application of the model

The developed mathematical model enables a quantitative understanding of copper concentrate oxidation under atmospheric conditions. This understanding offers multiple practical benefits in industrial settings:

- **Forecasting oxidation dynamics:** The model facilitates accurate prediction and monitoring of copper content depletion over time. This capability supports early detection of quality degradation during storage and transportation.

- **Process optimization:** By quantifying the influence of environmental factors (e.g., time, temperature, humidity), the model aids decision-making for optimizing storage protocols, handling methods, and transportation strategies.
- **Research extensibility:** The modeling framework lays a foundation for future integration into more complex microscale or mechanistic models by incorporating additional variables such as airborne contaminants, airflow patterns, or microbial activity, allowing for a more comprehensive understanding of oxidation under real-world conditions.

3.6. Limitations

The present study did not include molecular identification or detailed characterization of the bacterial strains isolated from the concentrate.

Additionally, the catalytic influence of trace Ag^+ was inferred indirectly from electrochemical and mineralogical observations rather than confirmed by micro-analytical evidence such as SEM–EDS or XPS. Future high-resolution analyses are recommended to verify this Ag-mediated pathway. Similarly, while preliminary culturing confirmed the presence of Acidithiobacillus-like organisms (Acidi-40, Acidi-41), molecular and genomic characterization remains incomplete. Future research will integrate microbiological assays with geochemical monitoring to more rigorously validate bacterial contributions to copper concentrate oxidation. Furthermore, the microbiological assays performed in this study were preliminary; detailed taxonomic identification of the Acidithiobacillus-like isolates and their long-term bio-oxidation behavior will be explored in future work.

Although the regression models provided strong predictive accuracy ($R^2 > 0.75$), certain mineralogical and physical factors were not fully incorporated as explicit predictors. For instance, the moisture retention capacity ($H_2O\%$) of the samples was determined experimentally, yet not directly included in the regression equations. Similarly, particle size distribution revealed that 54.6% of the material was finer than 44 µm, corresponding to increased surface area and greater sensitivity to humidity-driven processes. Other textural factors such as porosity, which were not directly quantified, may also have influenced RH sensitivity. Therefore, the RH coefficients particularly the contrasting RH effects observed in Sample-1 (negative) and Sample-2 (positive) should be interpreted as partially reflecting the correlated impacts of moisture retention, fine particle content, and porosity, rather than the independent effect of RH alone. These limitations highlight the need for future models to explicitly integrate such mineralogical parameters for more accurate prediction of humidity effects.

4. Conclusion

The atmospheric oxidation of copper concentrates proceeds through a multi-stage mechanism involving galvanic, biological, and chemical pathways. Experimental observations confirmed that environmental variables particularly storage duration and temperature play a dominant role in copper phase transformation and associated mass loss, while the influence of humidity depends on mineralogical composition.

To quantify these changes, a dual modeling approach incorporating multivariate linear regression and double-exponential fitting was applied. The models demonstrated strong predictive performance, with R^2 values exceeding 0.75, highlighting storage time as the most influential factor, followed by temperature. Relative humidity showed sample-dependent effects.

In addition to modeling, X-ray diffraction (XRD) analysis provided mineralogical evidence of oxidative phase transitions, including the degradation of chalcopyrite and formation of oxidized copper species. These mineralogical shifts aligned with trends observed in experimental data and supported the proposed oxidation mechanism.

The predictive models successfully captured these empirical oxidation patterns and enabled 3D visualization of copper depletion across different environmental scenarios. This integrated experimental-modeling framework offers a practical and scientifically rigorous approach for assessing oxidative behavior, guiding quality control, and optimizing storage and transportation strategies for copper concentrates under real-world conditions.

In summary, combining empirical evidence with mineralogical validation and predictive modeling yields a comprehensive foundation for anticipating and mitigating oxidation-induced copper loss, thereby supporting informed and resilient decision-making in copper concentrate logistics.

Funding sources

This research was funded by the Asian Research Center of the National University of Mongolia under Project No. P2025-5014, and by the Research Fund for the Research Assistantship Program (A/14-2025) of the National University of Mongolia.

Acknowledgment

The authors gratefully acknowledge the financial support provided by the Asian Research Center Foundation of the National University of Mongolia under Project No. P2025-5014, as well as the Research Fund for the Research Assistantship Program (A/14-2025) of the National University of Mongolia. We also express our gratitude to the Geological Center for Research and Analysis for providing necessary facilities and resources.

The authors acknowledge the contributions of accredited external laboratories for the determination of trace and major elements, as well as the efforts of the Central Geological Laboratory and RC Inspection for providing independent QA/QC validation. Additional wet-chemical and electrochemical analyses were performed at the National University of Mongolia. These collaborative efforts ensured the reliability and reproducibility of the datasets generated in this study.

REFERENCES

[1] Q. Yin, G.H. Kelsall, D.J. Vaughan, K.E.R. England, Atmospheric and electrochemical oxidation of the surface of chalcopyrite (CuFeS2). Geochim. Cosmochim. Acta **59** (6), 1091-1100 (1995). DOI: https://doi.org/10.1016/0016-7037(95)00026-v

[2] D.D. Rimstidt, D.J. Vaughan, Pyrite oxidation: A state-of-the-art assessment of the reaction mechanism. Geochim. Cosmochim. Acta **67** (5), 873-880 (2003). DOI: https://doi.org/10.1016/s0016-7037(02)01165-1

[3] H. Zhao et al., Role of pyrite in sulfuric acid leaching of chalcopyrite: An elimination of polysulfide by controlling redox potential. Hydrometallurgy **164**, 159-165 (2016). DOI: https://doi.org/10.1016/j.hydromet.2016.04.013

[4] A.P. Mehta, L.E. Murr, Kinetic Study of Sulfide Leaching By Galvanic Interaction Between Pyrite, Chalcopyrite, and Sphalerite in the Presence of Bacteria. Soc. Min. Eng. AIME **24** (4), 919-940, (1982). DOI: https://doi.org/10.1002/bit.260240413

[5] E.M. Córdoba, J.A. Muñoz, M.L. Blázquez, F. González, A. Ballester, Leaching of chalcopyrite with ferric ion. Part I: General aspects. Hydrometallurgy **93** (3-4), 81-87 (2008). DOI: https://doi.org/10.1016/j.hydromet.2008.04.015

[6] S.M.J. Koleini, M. Jafarian, M. Abdollahy, V. Aghazadeh, Galvanic leaching of chalcopyrite in atmospheric pressure and sulfate media: Kinetic and surface studies. Ind. Eng. Chem. Res. **49** (13), 5997-6002 (2010). DOI: https://doi.org/10.1021/ie100017u

[7] Y. Mu, Y. Peng, R.A. Lauten, The galvanic interaction between chalcopyrite and pyrite in the presence of lignosulfonate-based biopolymers and its effects on flotation performance. Miner. Eng. **122** (15), 91-98 (2018). DOI: https://doi.org/10.1016/j.mineng.2018.03.048

[8] D. Davaasambuu, Extraction, production and use of minerals and elements, 1nd ed. Mongolia: Press of Mongolian Science and Technology University, 2000.

[9] D. Erdenechimeg, Chemical technology non-ferrous and precious metals. 2st ed., in Mongolia: Press of National University of Mongolia, 2020.

[10] H.D.Z. Ekmekqi, Effects of galvanic interaction on collectorless flotation behaviour of chalcopyrite and pyrite. International Journal of Mineral Processing **52** (1), 31-48 (1997). DOI: https://doi.org/10.1016/S0301-7516(97)00050-1

[11] A.P. Chandra, A.R. Gerson, A review of the fundamental studies of the copper activation mechanisms for selective flotation of the sulfide minerals, sphalerite and pyrite. Adv. Colloid. Interface Sci. **145** (1-2), 97-110 (2009). DOI: https://doi.org/10.1016/j.cis.2008.09.001

[12] S.M.J. Koleini, V. Aghazadeh, Å. Sandström, Acidic sulphate leaching of chalcopyrite concentrates in presence of pyrite. Miner. Eng. **24** (5), 381-386 (2011). DOI: https://doi.org/10.1016/j.mineng.2010.11.008

[13] G. Debernardi, C. Carlesi, Chemical-electrochemical approaches to the study passivation of chalcopyrite. Miner. Process. Extra. Metall. Rev. **34** (1), 10-41 (2013). DOI: https://doi.org/10.1080/08827508.2011.623745

[14] T. Huang, D. Li, Presentation on mechanisms and applications of chalcopyrite and pyrite bioleaching in biohydrometallurgy – A presentation, Biotechnology Rep. **4** (1), 107-119 (2014). DOI: https://doi.org/10.1016/j.btre.2014.09.003

[15] Q.G. Zhou et al., Isolation of a strain of Acidithiobacillus caldus and its role in bioleaching of chalcopyrite. World J. Microbiol. Biotechnol. **23** (9), 1217-1225 (2007). DOI: http://doi.org/10.1007/s11274-007-9350-6

[16] W. Min Zeng et al., Isolation and identification of moderately thermophilic acidophilic iron-oxidizing bacterium and its bioleaching characterization. Trans. Nonferrous Met. Soc. China **19** (1), 222-227 (2009). DOI: https://doi.org/10.1016/S1003-6326(08)60256-3

[17] A. Chopard, B. Plante, M. Benzaazoua, H. Bouzahzah, P. Marion, Geochemical investigation of the galvanic effects during oxidation of pyrite and base-metals sulfides. Chemosphere **166**, 281-291 (2017). DOI: https://doi.org/10.1016/j.chemosphere.2016.09.129

[18] Y. Zhang et al., A brief overview on the dissolution mechanisms of sulfide minerals in acidic sulfate environments at low temperatures: Emphasis on electrochemical cyclic voltammetry analysis. Miner. Eng. **158** (932), 106586 (2020). DOI: https://doi.org/10.1016/j.mineng.2020.106586

[19] V.K. Berry, L.E. Murr, J.B. Hiskey, Galvanic interaction between chalcopyrite and pyrite during bacterial leaching of low-grade waste. Hydrometallurgy **3** (4), 309-326 (1978). DOI: https://doi.org/10.1016/0304-386x(78)90036-1

[20] H. Sato, H. Nakazawa, Y. Kudo, Effect of silver chloride on the bioleaching of chalcopyrite concentrate. International Journal of Mineral Processing **59** (1), 17-24 (2000). DOI: https://doi.org/10.1016/S0301-7516(99)00061-7

[21] M. Wang, Y. Zhang, T. Deng, K. Wang, Kinetic modeling for the bacterial leaching of chalcopyrite catalyzed by silver ions. Miner. Eng. **17** (7-8), 943-947 (2004). DOI: https://doi.org/10.1016/j.mineng.2003.11.021

[22] H. Zhao et al., The dissolution and passivation mechanism of chalcopyrite in bioleaching: An overview. Miner. Eng. **136** (932), 140-154 (2019). DOI: https://doi.org/10.1016/j.mineng.2019.03.014

[23] P.C. Banerjee, B.K. Chakrabarti, S. Bhattacharyya, A. Das, Technical Note Silver-catalysed hydrometallurgical extraction of copper from sulfide ores from Indian mines. Hydrometallurgy **25** (3), 349-355 (1990). DOI: https://doi.org/10.1016/0304-386x(90)90049-8

[24] J. Wang, H. Zhao, W. Qin, C. Yang, G. Qiu, Investigation of Interface Reactions and Electrochemical Behaviors of Chalcopyrite Dissolution in Different Leaching Mediums. International Journal of Electrochemical Science **8** (12), 12590-12599 (2013). DOI: https://doi.org/10.1016/s1452-3981(23)13291-3

[25] C.L. Liang et al., Characterization of the thermo-reduction process of chalcopyrite at 65°C by cyclic voltammetry and XANES spectroscopy. Hydrometallurgy **107** (1-2), 13-21 (2011). DOI: https://doi.org/10.1016/j.hydromet.2011.01.011

[26] D.G. Dixon, D.D. Mayne, K.G. Baxter, Galvanox^{TM} – A novel galvanically-assisted atmospheric leaching technology for copper concentrates. Can. Metall. Q **47** (3), 327-336 (2008). DOI: https://doi.org/10.1179/cmq.2008.47.3.327.

[27] N. Pradhan, K.C. Nathsarma, K. Srinivasa Rao, L.B. Sukla, B.K. Mishra, Heap bioleaching of chalcopyrite: A review. Miner. Eng. **21** (5), 355-365 (2008).
DOI: https://doi.org/10.1016/j.mineng.2007.10.018

[28] L.X. Xia et al., Relationships among bioleaching performance, additional elemental sulfur, microbial population dynamics and its energy metabolism in bioleaching of chalcopyrite. Transactions of Nonferrous Metals Society of China (English Edition), Eng. **22** (1), 192-198 (2012).
DOI: https://doi.org/10.1016/s1003-6326(11)61160-6

[29] Z.A.A.G.I. Karavaiko, G. Rossi, A.D Agate, S.N Groudev, Biogeotechnology of metals. Practical guide. Moscov: GKST (1988).

[30] M. Descostes, F. Mercier, N. Thromat, C. Beaucaire, M. Gautier-Soyer, Use of XPS in the determination of chemical environment and oxidation state of iron and sulfur samples: constitution of a data basis in binding energies for Fe and S reference compounds and applications to the evidence of surface species of an oxidized pyrite in a carbonate medium. Appl. Surf. Sci. **165** (4), 288-302 (2000). DOI: https://doi.org/10.1016/S0169-4332(00)00443-8

[31] A. Dakkoune et al., Hydrometallurgical Processing of Chalcopyrite by Attrition-Aided Leaching. ACS Engineering Au, **3** (3), 195-209 (2023). DOI: https://doi.org/10.1021/acsengineeringau.2c00051

[32] L. Li, I. Bergeron, A. Ghahreman, The effect of temperature on the kinetics of the ferric-ferrous redox couple on pyrite. Electrochim. Acta **245**, 814-828 (2017).
DOI: https://doi.org/10.1016/j.electacta.2017.05.198

[33] Alsin Fuambe Tshilombo, Mechanism and kinetics of chalcopyrite passivation and depassivation during ferric and microbial leaching. The University of British Columbia, 2004. [Online]. Available: https://open.library.ubc.ca/collections/831/items/1.0078957

[34] R. Cruz, R.M. Luna-Sánchez, G.T. Lapidus, I. González, M. Monroy, An experimental strategy to determine galvanic interactions affecting the reactivity of sulfide mineral concentrates. Hydrometallurgy **78** (3-4), 198-208 (2005).
DOI: https://doi.org/10.1016/j.hydromet.2005.03.006

SUPPLEMENTARY

Information

TABLE S1

Major elemental compositions of copper concentrate sample 1-N during the four-month monitoring period (May-September)

No.	Date	t^0, C	Humidity, %	H_2O, %	Cu, %	S, %	Fe, %	Zn,%	SiO_2,%	CaO,%	Icorr	Ecorr	pH
1	**2**	**3**	**4**	**5**	**6**	**7**	**8**	**9**	**10**	**11**	**12**	**13**	**14**
1	V/14	13	44	8.577	24.58	32.31	26.44	0.10	8.37	0.60	2.0429	0.080	7.07
2	V/17	24	10	8.464	24.63	30.98	25.97	0.11	8.49	0.60	2.3578	0.095	7.00
3	V/20	26	9	8.450	24.56	32.95	27.43	0.12	8.90	0.64	2.7220	0.175	6.60
4	V/23	8	24	8.292	24.49	31.45	26.02	0.11	8.53	0.62	2.2916	0.030	6.62
5	V/26	14	32	8.318	24.48	31.41	26.17	0.11	8.61	0.62	1.8934	0.020	6.56
6	V/29	20	28	8.090	24.52	31.88	26.08	0.11	8.45	0.62	2.0902	0.030	6.52
7	VI/1	14	24	7.794	24.54	31.62	27.56	0.11	8.80	0.64	2.8714	0.085	6.63
8	VI/4	17	38	7.940	24.47	32.19	27.09	0.10	8.63	0.62	2.0205	0.080	6.50
9	VI/7	21	50	7.341	24.43	32.05	27.70	0.11	8.45	0.61	1.0355	0.005	6.47
10	VI/10	23	18	7.125	24.31	32.47	27.91	0.11	8.65	0.63	1.1551	0.010	5.91
11	VI/13	21	52	6.100	24.37	32.03	25.46	0.11	8.83	0.64	0.8945	0.040	4.06
12	VI/16	18	51	8.642	24.41	31.86	27.63	0.11	8.63	0.61	0.1494	0.030	4.12
13	VI/19	22	20	7.201	24.38	33.60	26.82	0.11	8.63	0.62	0.9355	0.040	4.10
14	VI/22	26	25	6.942	24.42	32.13	26.79	0.11	8.43	0.61	2.7628	0.085	3.30
15	VI/25	25	28	6.887	24.41	31.55	26.38	0.11	8.70	0.63	2.2671	0.135	3.70
16	VI/28	29	21	5.908	24.29	31.07	26.38	0.11	8.64	0.65	2.2592	0.160	2.85
17	VII/01	19	34	5.184	24.08	32.65	26.72	0.11	8.42	0.64	2.8279	0.225	4.42
18	VII/04	22	46	5.846	24.16	31.77	26.15	0.11	8.56	0.62	3.1589	0.185	3.51
19	VII/07	28	24	7.047	24.03	33.68	26.08	0.11	8.46	0.64	2.1688	0.075	3.70
20	VII/10	27	37	6.513	24.11	32.57	26.12	0.10	8.59	0.61	3.2471	0.215	3.36
21	VII/13	26	33	4.598	24.11	31.72	26.96	0.11	8.60	0.60	2.0842	0.170	3.36
22	VII/16	29	26	8.711	24.03	31.83	27.65	0.11	8.68	0.61	1.6540	0.105	3.42
23	VII/19	33	22	6.103	24.04	32.15	26.42	0.10	8.50	0.62	0.5308	0.045	3.15
24	VII/22	27	49	5.197	24.00	32.52	27.63	0.10	8.43	0.60	1.0347	0.075	2.83

TABLE S1. Continued

1	2	3	4	5	6	7	8	9	10	11	12	13	14
25	VII/25	18	90	5.401	23.93	32.15	28.23	0.10	8.52	0.61	0.9548	0.045	3.02
26	VII/28	23	55	10.374	23.91	31.69	27.25	0.09	8.60	0.58	1.4547	0.065	2.92
27	VII/31	18	56	10.970	23.97	31.90	26.59	0.09	8.49	0.57	1.7888	0.125	3.24
28	VIII/03	22	34	6.208	24.01	32.59	27.26	0.11	8.36	0.58	1.7888	0.055	2.82
29	VIII/07	24	26	6.955	23.93	32.17	25.66	0.12	8.49	0.59	0.0652	0.060	2.94
30	VIII/14	23	34	5.340	23.91	31.80	25.84	0.12	8.35	0.61	3.3440	0.125	3.84
31	VIII/21	25	34	8.413	23.71	30.98	26.45	0.10	8.43	0.56	2.9353	0.220	3.70
32	VIII/28	15	62	8.64	23.84	32.80	26.35	0.11	8.46	0.59	3.1248	0.160	3.96
33	IX/04	17	63	5.474	23.86	31.63	27.00	0.12	8.30	0.59	2.6560	0.800	3.94
34	IX/11	19	38	7.737	23.62	31.15	27.56	0.10	8.51	0.59	3.5704	0.135	3.88
35	IX/18	17	35	6.927	23.67	31.50	26.4	0.12	8.37	0.58	1.1636	0.125	3.84

Values include Cu, Fe, S, Zn, SiO_2, CaO, H_2O%, pH, and electrochemical parameters (Icorr, Ecorr). Sampling and analyses were carried out every three days from May to August, while in September, sampling was performed once per week to monitor oxidation.

TABLE S2

Major elemental compositions of copper concentrate sample 2-N during the four-month monitoring period (May-September)

No.	Date	t^0, C	Humidity, %	H_2O, %	Cu, %	S, %	Fe, %	Zn,%	SiO_2,%	CaO,%	Icorr	Ecorr	pH
1	V/14	13	44	8.486	21.09	35.32	28.92	0.22	7.73	0.44	4.0710	0.320	7.30
2	V/17	24	10	8.295	20.78	36.77	29.24	0.22	7.85	0.43	4.8491	0.105	6.33
3	V/20	26	9	8.325	20.78	34.25	29.45	0.22	7.96	0.45	2.9046	0.050	6.59
4	V/23	8	24	8.143	20.62	34.93	30.22	0.22	7.73	0.47	1.8197	-0.010	6.53
5	V/26	14	32	8.131	20.90	35.74	28.45	0.22	7.82	0.45	1.3668	0.065	6.51
6	V/29	20	28	7.905	20.84	36.53	30.78	0.22	7.68	0.44	1.8214	-0.010	6.53
7	VI/1	14	24	7.622	21.12	35.94	30.52	0.23	8.03	0.47	1.5819	-0.065	6.54
8	VI/4	17	38	7.718	20.81	33.15	27.59	0.22	7.95	0.46	1.5955	-0.010	6.52
9	VI/7	21	50	7.397	20.91	34.51	28.71	0.23	7.96	0.45	1.2503	0.000	6.56
10	VI/10	23	18	7.162	20.67	33.60	31.85	0.22	7.83	0.46	1.2062	0.030	5.30
11	VI/13	21	52	6.838	20.87	35.08	28.30	0.22	7.94	0.45	2.6730	-0.055	4.09
12	VI/16	18	51	6.733	20.82	34.64	29.35	0.22	7.83	0.46	0.3718	0.055	4.07
13	VI/19	22	20	6.045	20.78	33.89	28.89	0.22	8.04	0.46	4.0710	0.195	3.86
14	VI/22	26	25	6.660	20.67	36.17	29.75	0.22	7.80	0.45	3.0230	0.205	2.80
15	VI/25	25	28	6.410	20.69	34.66	29.44	0.22	7.78	0.44	3.1248	0.185	3.44
16	VI/28	29	21	5.892	20.60	33.20	28.68	0.22	7.52	0.42	2.4341	0.230	2.73
17	VII/01	19	34	4.366	20.54	35.39	28.89	0.21	7.74	0.45	2.5591	0.185	3.29
18	VII/04	22	46	4.600	20.55	36.41	28.44	0.21	7.85	0.45	2.7419	0.165	3.28
19	VII/07	28	24	5.836	20.38	34.65	28.25	0.22	7.84	0.41	1.2514	0.230	3.40
20	VII/10	27	37	5.650	20.53	33.65	28.70	0.21	7.80	0.44	3.3176	0.110	3.28
21	VII/13	26	33	5.616	20.49	34.28	29.12	0.21	7.66	0.42	2.6477	0.095	3.22
22	VII/16	29	26	5.066	20.45	35.24	29.23	0.20	7.62	0.44	3.0040	0.230	3.29
23	VII/19	33	22	4.862	20.49	35.00	29.60	0.27	7.76	0.45	0.9301	0.025	2.60
24	VII/22	27	49	5.016	20.52	33.93	29.30	0.20	7.43	0.43	0.5405	0.025	2.75
25	VII/25	18	90	6.127	20.39	34.59	29.97	0.20	7.86	0.45	0.9670	-0.035	2.62
26	VII/28	23	55	5.198	20.46	34.34	29.47	0.20	7.75	0.43	1.0044	0.115	2.86
27	VII/31	18	56	8.272	20.56	34.20	29.59	0.20	7.94	0.43	1.5273	0.070	3.50
28	VIII/03	22	34	4.228	20.49	34.95	29.64	0.22	7.80	0.44	1.1832	0.070	2.61
29	VIII/07	24	26	5.156	20.47	35.26	28.49	0.22	7.68	0.43	0.8126	0.055	2.87
30	VIII/14	23	34	8.830	20.37	33.88	27.97	0.22	7.73	0.43	1.2879	0.090	3.61
31	VIII/21	25	34	5.545	20.40	32.71	28.87	0.23	7.89	0.45	1.8882	0.115	3.75
32	VIII/28	15	62	8.429	20.34	34.14	29.40	0.20	7.90	0.43	4.1501	0.370	3.76
33	IX/04	17	63	6.476	20.41	35.02	28.41	0.22	7.55	0.42	2.8117	0.230	3.74
34	IX/11	19	38	6.752	20.46	33.96	30.44	0.2	7.81	0.45	2.9817	0.135	3.65
35	IX/18	17	35	5.392	20.31	33.37	29.12	0.22	7.65	0.42	3.2115	0.120	3.72

TABLE S3

Phase-resolved copper speciation results for sample 1-N during the monitoring period

Date	Cu(ox),%	Cu(II),%	Cu(I),%	Cu(total),%	pH	t^0, C	Humidity, %
V/14	0.10	6.38	18.51	24.58	7.07	13	44
V/17	0.31	6.31	18.41	24.63	7.00	24	10
V/20	0.28	6.28	18.36	24.56	6.6	26	9
V/23	0.28	6.17	18.57	24.49	6.62	8	24
VI/01	0.45	6.48	18.42	24.56	6.63	14	24
VI/16	0.58	6.41	18.05	24.5	4.12	18	51
VII/01	0.68	5.72	17.68	24.08	4.42	19	34
VII/16	0.80	5.77	17.55	24.13	3.42	29	26
VII/31	0.76	5.80	17.47	23.97	3.24	18	56
VIII/14	0.89	5.58	17.95	23.91	3.84	23	34
IX/04	0.97	5.45	17.32	23.86	3.94	16	63
IX/18	1.06	5.33	17.18	23.3	3.84	17	35

The relative proportions of Cu(I), Cu(II), and Cu(ox) were quantified at selected timepoints together with pH measurements, highlighting temporal variations in phase transformation trends.

TABLE S4

Phase-resolved copper speciation results for sample 2-N during the monitoring period

Date	Cu(ox),%	Cu(II),%	Cu(I),%	Cu(total),%	pH	t^0, C	Humidity, %
V/14	0.11	4.61	16.95	21.17	7.30	13	44
V/17	0.21	4.46	16.63	20.78	6.33	24	10
V/20	0.20	4.22	16.89	20.78	6.59	26	9
V/23	0.22	4.23	16.68	20.62	6.53	8	24
VI/1	0.28	4.20	16.52	20.96	6.54	14	24
VI/16	0.32	4.08	16.31	20.96	4.07	18	51
VII/1	0.55	4.15	16.12	20.69	3.29	19	34
VII/16	0.62	4.00	15.80	20.59	3.29	29	26
VII/31	0.76	4.04	16.27	20.56	3.5	18	56
VIII/14	0.87	3.01	16.20	20.37	3.61	23	34
IX/04	1.04	2.73	15.94	20.41	3.74	16	63
IX/18	1.13	2.76	15.68	20.31	3.72	17	35

Parameters include Cu(I), Cu(II), Cu(ox), Cu(total), and pH at multiple timepoints. Replicate analyses support the evaluation of oxidation pathways.

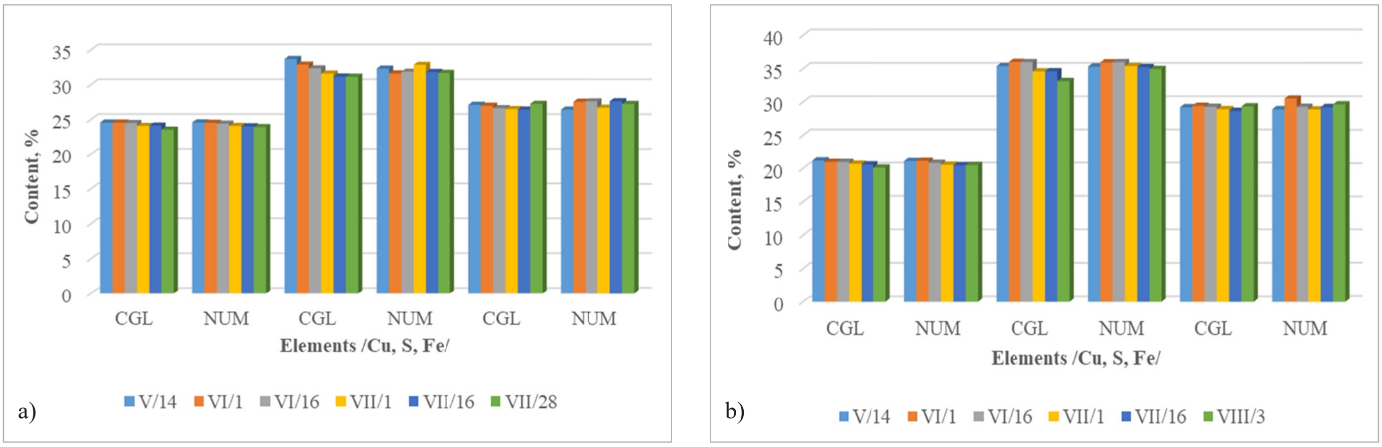

Fig. S1. Inter-laboratory comparison of Cu, S, and Fe contents in copper concentrate samples (L-1-N and L-2-N)

Analyses were performed independently by the Central Geological Laboratory (CGL), RC Inspection, and the National University of Mongolia (NUM) across multiple timepoints. Error bars represent triplicate determinations, demonstrating reproducibility and cross-laboratory consistency.

TABLE S5

Comprehensive elemental compositions of copper concentrate samples (1-N and 2-N)

METHOD	AAS	AAS	XRF	XRF	ICP-MS	ICP-MS	XRF	ICP-MS	XRF	ICP-MS	XRF	XRF	XRF	XRF	XRF	XRF
COMPONENT	Au	Ag	Al_2O_3	As	Ba	Bi	CaO	Cd	Co	Cr	Cu	Fe	K_2O	MgO	MnO	Mo
DESCRIPTION	mg/kg	mg/kg	%	%	%	%	%	%	%	%	%	%	%	%	%	%
10240-N 17 May	37.25	52.57	2.65	0.05	0.0060	0.0016	0.60	0.00192	0.02	0.00193	24.63	25.97	0.56	0.82	0.0387	0.29
10241-N 17 May	29.96	43.19	2.44	0.06	0.0064	0.0010	0.43	0.00241	0.02	0.00169	20.78	29.24	0.49	0.65	0.0258	0.20
10240-N 20 May	37.25	52.57	2.77	0.09	0.0060	0.0016	0.64	0.00192	0.01	0.00193	24.56	27.43	0.57	0.77	0.0387	0.28
10241-N 20 May	29.96	43.19	2.48	0.09	0.0064	0.0010	0.45	0.00241	0.01	0.00169	20.78	29.45	0.51	0.69	0.0258	0.21
10240-N 23 May	37.25	52.57	2.67	0.05	0.0060	0.0016	0.62	0.00192	0.01	0.00193	24.49	26.02	0.57	0.82	0.0258	0.25
10241-N 23 May	29.96	43.19	2.49	0.10	0.0064	0.0010	0.47	0.00241	0.02	0.00169	20.62	30.22	0.50	0.71	0.0387	0.20
10240-N 26 May	37.25	52.57	2.72	0.05	0.0060	0.0016	0.62	0.00192	0.01	0.00193	24.48	26.17	0.57	0.94	0.0387	0.26
10241-N 26 May	29.96	43.19	2.56	0.10	0.0064	0.0010	0.45	0.00241	0.02	0.00169	20.90	28.45	0.50	0.74	0.0258	0.20
10240-N 29 May	37.25	52.57	2.69	0.04	0.0060	0.0016	0.62	0.00192	0.01	0.00193	24.52	26.08	0.56	0.89	0.0258	0.23
10241-N 29 May	29.96	43.19	2.52	0.07	0.0064	0.0010	0.44	0.00241	0.01	0.00169	20.84	30.78	0.51	0.73	0.0258	0.21
10240-N 01 June	37.25	52.57	2.81	0.03	0.0060	0.0016	0.64	0.00192	0.02	0.00193	24.54	27.56	0.58	0.89	0.0258	0.27
10241-N 01.June	29.96	43.19	2.56	0.09	0.0064	0.0010	0.47	0.00241	0.02	0.00169	21.12	30.52	0.52	0.69	0.0258	0.20
10240-N 07.June	37.25	52.57	2.71	0.04	0.0060	0.0016	0.61	0.00192	0.02	0.00193	24.43	27.70	0.55	0.86	0.0258	0.25
10241-N 07.June	29.96	43.19	2.52	0.09	0.0064	0.0010	0.45	0.00241	0.02	0.00169	20.91	28.71	0.51	0.71	0.0258	0.19
10240-N 11.June	37.25	52.57	2.72	0.01	0.0060	0.0016	0.63	0.00192	0.01	0.00193	24.31	27.91	0.55	0.85	0.0258	0.24
10241-N 11.June	29.96	43.19	2.51	0.07	0.0064	0.0010	0.46	0.00241	0.02	0.00169	20.67	31.85	0.50	0.68	0.0258	0.21
10240-N 13.June	37.25	52.57	2.72	0.04	0.0060	0.0016	0.64	0.00192	0.01	0.00193	24.37	25.46	0.56	0.92	0.0258	0.24
10241-N 13.June	29.96	43.19	2.50	0.05	0.0064	0.0010	0.45	0.00241	0.01	0.00169	20.87	28.30	0.51	0.70	0.0258	0.19
10240-N 17.June	37.25	52.57	2.79	0.02	0.0060	0.0016	0.61	0.00192	0.01	0.00193	24.41	27.63	0.57	0.95	0.0258	0.23
10241-N 17.June	29.96	43.19	2.60	0.08	0.0064	0.0010	0.46	0.00241	0.02	0.00169	20.82	29.35	0.50	0.66	0.0258	0.21
10240-N 19.June	37.25	52.57	2.60	0.01	0.0060	0.0016	0.62	0.00192	0.01	0.00193	24.38	26.82	0.56	0.80	0.0258	0.25
10241-N 19.June	29.96	43.19	2.58	0.07	0.0064	0.0010	0.46	0.00241	0.02	0.00169	20.78	28.89	0.50	0.75	0.0258	0.19
10240-N 22 June	37.25	52.57	2.69	0.05	0.0060	0.0016	0.61	0.00192	0.02	0.00193	24.42	26.79	0.54	0.82	0.0258	0.28
10241-N 22 June	29.96	43.19	2.51	0.07	0.0064	0.0010	0.45	0.00241	0.01	0.00169	20.67	29.75	0.50	0.66	0.0258	0.20
10240-N 25 June	37.25	52.57	2.71	0.04	0.0060	0.0016	0.63	0.00192	0.02	0.00193	24.41	26.38	0.54	0.86	0.0258	0.26
10241-N 25 June	29.96	43.19	2.46	0.05	0.0064	0.0010	0.44	0.00241	0.01	0.00169	20.69	29.44	0.50	0.64	0.0258	0.19
10240-N 28 June	37.25	52.57	2.77	0.05	0.0060	0.0016	0.65	0.00192	0.02	0.00193	24.4	26.92	0.56	0.86	0.0258	0.26
10241-N 28 June	29.96	43.19	2.42	0.07	0.0064	0.0010	0.42	0.00241	0.02	0.00169	20.65	29.32	0.48	0.66	0.0258	0.18
10240-N 1 July	37.25	52.57	2.70	0.03	0.0060	0.0016	0.64	0.00192	0.01	0.00193	24.08	26.72	0.57	0.83	0.0387	0.24
10241-N 1 July	29.96	43.19	2.50	0.08	0.0064	0.0010	0.45	0.00241	0.01	0.00169	20.54	28.89	0.48	0.56	0.0258	0.19
10240-N 4 July	37.25	52.57	2.67	0.02	0.0060	0.0016	0.62	0.00192	0.01	0.00193	24.16	26.15	0.55	0.84	0.0387	0.27
10241-N 4 July	29.96	43.19	2.52	0.10	0.0064	0.0010	0.45	0.00241	0.02	0.00169	20.55	28.44	0.50	0.62	0.0258	0.21
10240-N 7 July	37.25	52.57	2.77	0.04	0.0060	0.0016	0.64	0.00192	0.01	0.00193	24.03	26.08	0.56	0.82	0.0258	0.25
10241-N 7 July	29.96	43.19	2.49	0.05	0.0064	0.0010	0.41	0.00241	0.01	0.00169	20.38	28.25	0.49	0.69	0.0258	0.19
10240-N 10 July	37.25	52.57	2.67	0.02	0.0060	0.0016	0.61	0.00192	0.01	0.00193	24.11	26.12	0.56	0.87	0.0387	0.25
10241-N 10 July	29.96	43.19	2.44	0.08	0.0064	0.0010	0.44	0.00241	0.02	0.00169	20.53	28.7	0.49	0.65	0.0258	0.19
10240-N 13 July	37.25	52.57	2.69	0.02	0.0060	0.0016	0.6	0.00192	0.01	0.00193	24.11	26.96	0.56	0.91	0.0387	0.24
10241-N 13 July	29.96	43.19	2.55	0.08	0.0064	0.0010	0.42	0.00241	0.01	0.00169	20.49	29.12	0.48	0.63	0.0258	0.22
10240-N 16 July	37.25	52.57	2.74	0.02	0.0060	0.0016	0.61	0.00192	0.01	0.00193	24.03	27.65	0.55	0.83	0.0387	0.24
10241-N 16 July	29.96	43.19	2.45	0.08	0.0064	0.0010	0.44	0.00241	0.01	0.00169	20.45	30.23	0.49	0.70	0.0258	0.19
10240-N 20 July	37.25	52.57	2.74	0.05	0.0060	0.0016	0.62	0.00192	0.01	0.00193	24.04	26.42	0.56	0.83	0.0387	0.25
10241-N 20 July	29.96	43.19	2.52	0.08	0.0064	0.0010	0.45	0.00241	0.01	0.00169	20.49	29.6	0.51	0.66	0.0258	0.18
10240-N 22 July	37.25	52.57	2.70	0.05	0.0060	0.0016	0.6	0.00192	0.01	0.00193	24.00	27.63	0.55	0.83	0.0258	0.23
10241-N 22 July	29.96	43.19	2.52	0.08	0.0064	0.0010	0.43	0.00241	0.01	0.00169	20.52	29.3	0.48	0.60	0.0258	0.16
10240-N 25 July	37.25	52.57	2.78	0.03	0.0060	0.0016	0.61	0.00192	0.01	0.00193	23.93	28.23	0.54	0.79	0.0258	0.24
10241-N 25 July	29.96	43.19	2.56	0.08	0.0064	0.0010	0.45	0.00241	0.01	0.00169	20.39	29.97	0.52	0.69	0.0258	0.21
10240-N 28 July	37.25	52.57	2.74	0.05	0.0060	0.0016	0.58	0.00192	0.01	0.00193	23.91	27.25	0.56	0.84	0.0258	0.27
10241-N 28 July	29.96	43.19	2.59	0.09	0.0064	0.0010	0.43	0.00241	0.01	0.00169	20.46	29.47	0.47	0.69	0.0258	0.18
10240-N 31 July	37.25	52.57	2.75	0.03	0.0060	0.0016	0.57	0.00192	0.01	0.00193	23.97	26.59	0.55	0.82	0.0258	0.22
10241-N 31 July	29.96	43.19	2.64	0.09	0.0064	0.0010	0.43	0.00241	0.02	0.00169	20.56	29.59	0.49	0.70	0.0258	0.22
10240-N 3 Aug	37.25	52.57	2.65	0.01	0.0060	0.0016	0.58	0.00192	0.01	0.00193	24.01	27.26	0.53	0.81	0.0258	0.25
10241-N 3 Aug	29.96	43.19	2.56	0.09	0.0064	0.0010	0.44	0.00241	0.01	0.00169	20.49	29.64	0.49	0.65	0.0258	0.20
10240-N 7 Aug	37.25	52.57	2.65	0.02	0.0060	0.0016	0.59	0.00192	0.01	0.00193	23.93	25.66	0.55	0.82	0.0258	0.25
10241-N 7 Aug	29.96	43.19	2.48	0.08	0.0064	0.0010	0.43	0.00241	0.01	0.00169	20.47	28.49	0.50	0.63	0.0258	0.18

TABLE S5. (Continued)

XRF	ICP-MS	XRF	XRF	XRF	ICP-MS	ICP-MS	XRF	ICP-MS	ICP-MS	XRF	XRF	XRF	ICP-MS	XRF	ICP-MS
Nb	Ni	P_2O_5	Pb	S	Sb	Se	SiO_2	Sn	Sr	Ta	TiO_2	V	WO_3	Zn	Zr
%	%	%	%	%	%	%	%	%	%	%	%	%	%	%	%
0.01	0.00331	0.0687	0.06	30.98	0.0018	0.0332	8.49	0.00033	0.00655	0.01	0.41	0.01	0.000145	0.11	0.0009
0.01	0.00418	0.0687	0.08	36.77	0.0019	0.0273	7.85	0.00044	0.00628	0.01	0.44	0.01	0.000136	0.22	0.0010
0.02	0.00331	0.0687	0.07	32.95	0.0018	0.0332	8.90	0.00033	0.00655	0.02	0.37	0.01	0.000145	0.12	0.0009
0.01	0.00418	0.0687	0.08	34.25	0.0019	0.0273	7.96	0.00044	0.00628	0.01	0.36	0.01	0.000136	0.22	0.0010
0.01	0.00331	0.0687	0.06	31.45	0.0018	0.0332	8.53	0.00033	0.00655	0.01	0.38	0.01	0.000145	0.11	0.0009
0.01	0.00418	0.0687	0.09	34.93	0.0019	0.0273	7.73	0.00044	0.00628	0.01	0.39	0.01	0.000136	0.22	0.0010
0.01	0.00331	0.0917	0.06	31.45	0.0018	0.0332	8.61	0.00033	0.00655	0.02	0.38	0.01	0.000145	0.11	0.0009
0.01	0.00418	0.0687	0.09	32.74	0.0019	0.0273	7.82	0.00044	0.00628	0.02	0.35	0.01	0.000136	0.22	0.0010
0.01	0.00331	0.0687	0.06	31.88	0.0018	0.0332	8.45	0.00033	0.00655	0.01	0.41	0.01	0.000145	0.11	0.0009
0.01	0.00418	0.0687	0.08	35.53	0.0019	0.0273	7.68	0.00044	0.00628	0.01	0.36	0.01	0.000136	0.22	0.0010
0.02	0.00331	0.0687	0.06	30.62	0.0018	0.0332	8.80	0.00033	0.00655	0.02	0.37	0.01	0.000145	0.11	0.0009
0.02	0.00418	0.0687	0.10	31.94	0.0019	0.0273	8.03	0.00044	0.00628	0.01	0.37	0.01	0.000136	0.23	0.0010
0.02	0.00331	0.0687	0.06	32.05	0.0018	0.0332	8.45	0.00033	0.00655	0.01	0.37	0.01	0.000145	0.11	0.0009
0.02	0.00418	0.0687	0.10	34.51	0.0019	0.0273	7.96	0.00044	0.00628	0.02	0.36	0.02	0.000136	0.23	0.0010
0.01	0.00331	0.0687	0.06	32.47	0.0018	0.0332	8.65	0.00033	0.00655	0.01	0.37	0.01	0.000145	0.11	0.0009
0.01	0.00418	0.0917	0.09	33.60	0.0019	0.0273	7.83	0.00044	0.00628	0.01	0.39	0.01	0.000136	0.22	0.0010
0.01	0.00331	0.0687	0.06	32.03	0.0018	0.0332	8.83	0.00033	0.00655	0.01	0.41	0.01	0.000145	0.11	0.0009
0.01	0.00418	0.0687	0.09	35.08	0.0019	0.0273	7.94	0.00044	0.00628	0.01	0.42	0.01	0.000136	0.22	0.0010
0.03	0.00331	0.0687	0.06	31.86	0.0018	0.0332	8.63	0.00033	0.00655	0.01	0.4	0.01	0.000145	0.11	0.0009
0.01	0.00418	0.0687	0.09	32.64	0.0019	0.0273	7.83	0.00044	0.00628	0.01	0.44	0.01	0.000136	0.22	0.0010
0.01	0.00331	0.0917	0.06	33.60	0.0018	0.0332	8.63	0.00033	0.00655	0.01	0.43	0.01	0.000145	0.11	0.0009
0.01	0.00418	0.0687	0.09	33.89	0.0019	0.0273	8.04	0.00044	0.00628	0.01	0.4	0.01	0.000136	0.22	0.0010
0.01	0.00331	0.0687	0.06	32.13	0.0018	0.0332	8.43	0.00033	0.00655	0.01	0.41	0.01	0.000145	0.11	0.0009
0.01	0.00418	0.0687	0.07	36.17	0.0019	0.0273	7.80	0.00044	0.00628	0.01	0.44	0.01	0.000136	0.22	0.0010
0.02	0.00331	0.0687	0.06	31.55	0.0018	0.0332	8.70	0.00033	0.00655	0.02	0.44	0.01	0.000145	0.11	0.0009
0.01	0.00418	0.0687	0.08	32.66	0.0019	0.0273	7.78	0.00044	0.00628	0.01	0.45	0.01	0.000136	0.22	0.0010
0.02	0.00331	0.0917	0.06	32.72	0.0018	0.0332	8.64	0.00033	0.00655	0.02	0.39	0.01	0.000145	0.11	0.0009
0.01	0.00418	0.0687	0.08	33.04	0.0019	0.0273	7.52	0.00044	0.00628	0.01	0.39	0.01	0.000136	0.22	0.0010
0.02	0.00331	0.0687	0.06	32.85	0.0018	0.0332	8.42	0.00033	0.00655	0.01	0.4	0.01	0.000145	0.11	0.0009
0.01	0.00418	0.0687	0.08	29.59	0.0019	0.0273	7.74	0.00044	0.00628	0.01	0.41	0.01	0.000136	0.21	0.0010
0.01	0.00331	0.0687	0.05	31.77	0.0018	0.0332	8.56	0.00033	0.00655	0.01	0.4	0.01	0.000145	0.11	0.0009
0.01	0.00418	0.0917	0.08	38.41	0.0019	0.0273	7.85	0.00044	0.00628	0.01	0.48	0.01	0.000136	0.21	0.0010
0.01	0.00331	0.0687	0.05	33.68	0.0018	0.0332	8.46	0.00033	0.00655	0.01	0.41	0.01	0.000145	0.11	0.0009
0.01	0.00418	0.0917	0.07	34.65	0.0019	0.0273	7.84	0.00044	0.00628	0.01	0.41	0.01	0.000136	0.22	0.0010
0.01	0.00331	0.0687	0.06	32.57	0.0018	0.0332	8.59	0.00033	0.00655	0.01	0.47	0.01	0.000145	0.1	0.0009
0.02	0.00418	0.0687	0.08	33.65	0.0019	0.0273	7.80	0.00044	0.00628	0.01	0.41	0.01	0.000136	0.21	0.0010
0.01	0.00331	0.0687	0.06	31.72	0.0018	0.0332	8.60	0.00033	0.00655	0.01	0.47	0.01	0.000145	0.11	0.0009
0.01	0.00418	0.0917	0.08	34.28	0.0019	0.0273	7.66	0.00044	0.00628	0.01	0.48	0.01	0.000136	0.21	0.0010
0.01	0.00331	0.0687	0.06	32.83	0.0018	0.0332	8.68	0.00033	0.00655	0.01	0.46	0.01	0.000145	0.11	0.0009
0.02	0.00418	0.0917	0.07	35.24	0.0019	0.0273	7.62	0.00044	0.00628	0.01	0.47	0.01	0.000136	0.2	0.0010
0.01	0.00331	0.0687	0.05	32.15	0.0018	0.0332	8.50	0.00033	0.00655	0.01	0.42	0.01	0.000145	0.1	0.0009
0.01	0.00418	0.0917	0.08	35.00	0.0019	0.0273	7.76	0.00044	0.00628	0.01	0.4	0.01	0.000136	0.27	0.0010
0.01	0.00331	0.0917	0.06	32.52	0.0018	0.0332	8.43	0.00033	0.00655	0.01	0.4	0.01	0.000145	0.1	0.0009
0.02	0.00418	0.0687	0.08	33.93	0.0019	0.0273	7.43	0.00044	0.00628	0.01	0.4	0.01	0.000136	0.2	0.0010
0.01	0.00331	0.0917	0.06	32.15	0.0018	0.0332	8.52	0.00033	0.00655	0.01	0.48	0.01	0.000145	0.1	0.0009
0.02	0.00418	0.0917	0.08	34.59	0.0019	0.0273	7.86	0.00044	0.00628	0.01	0.42	0.01	0.000136	0.2	0.0010
0.01	0.00331	0.0687	0.05	31.69	0.0018	0.0332	8.60	0.00033	0.00655	0.01	0.37	0.01	0.000145	0.09	0.0009
0.02	0.00418	0.0687	0.08	34.34	0.0019	0.0273	7.75	0.00044	0.00628	0.01	0.43	0.01	0.000136	0.2	0.0010
0.02	0.00331	0.0917	0.06	31.90	0.0018	0.0332	8.49	0.00033	0.00655	0.01	0.35	0.01	0.000145	0.09	0.0009
0.01	0.00418	0.0687	0.08	34.20	0.0019	0.0273	7.94	0.00044	0.00628	0.01	0.37	0.01	0.000136	0.2	0.0010
0.02	0.00331	0.0687	0.05	32.59	0.0018	0.0332	8.36	0.00033	0.00655	0.01	0.39	0.01	0.000145	0.11	0.0009
0.02	0.00418	0.0917	0.08	34.95	0.0019	0.0273	7.80	0.00044	0.00628	0.01	0.41	0.01	0.000136	0.22	0.0010
0.01	0.00331	0.0687	0.05	32.17	0.0018	0.0332	8.49	0.00033	0.00655	0.01	0.39	0.01	0.000145	0.12	0.0009
0.01	0.00418	0.0687	0.08	35.26	0.0019	0.0273	7.68	0.00044	0.00628	0.01	0.44	0.01	0.000136	0.22	0.0010

Trace element compositions of copper concentrate samples (1-N and 2-N). Data were generated using multiple analytical techniques (AAS, ICP-MS/OES, XRF), covering both major and trace elements. These results provide a comprehensive characterization of elemental constituents in the two samples. From this dataset, the principal elements (Cu, Fe, S, etc.) were further determined and validated by the National University of Mongolia (NUM) laboratory for the purposes of the present study.

TABLE S6

Bulk chemical assays of trace elements in copper concentrate samples (Au, Ag, Zn, Pb, Ti)

Sample No.	**Day/month**	**Bulk concentration of selected trace elements (%)**				
		Au	**Ag**	**Zn**	**Pb**	**Ti**
1-N	14-May	0.0037	0.0053	0.11	0.06	0.24
2-N	14-May	0.0030	0.0043	0.22	0.08	0.26

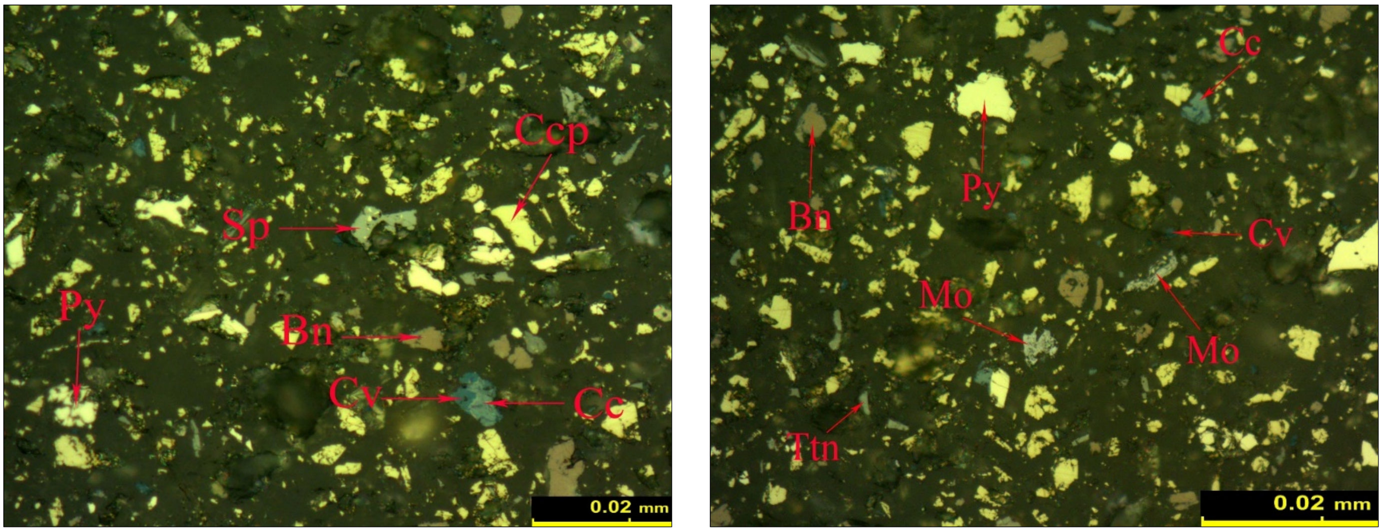

Fig. S2. Reflected-light photomicrographs (500×) of polished sections showing chalcopyrite (Cp), pyrite (Py), covellite (Cv), bornite (Bn), molybdenite (Mo), titanite (Ttn), and sphalerite (Sp). No discrete Ag-bearing phases were observed

Figure S2

Polished briquettes prepared from the concentrate were examined by reflected-light microscopy. The dominant identified sulfide minerals were chalcopyrite, pyrite, covellite, bornite, sphalerite, molybdenite, and titanite. Chalcopyrite occurred as yellowish grains intergrown with pyrite, covellite, and bornite. Pyrite appeared as pale yellow cubic and granular crystals. Bornite was seen as brownish aggregates, commonly associated with chalcopyrite. Covellite was present as blue, platy aggregates replacing chalcopyrite and bornite. Molybdenite occurred as silvery-gray flakes intergrown with chalcopyrite and pyrite. Titanite appeared as reddish-brown grains, typically associated with gangue phases. No optically resolvable Ag-bearing minerals were detected, consistent with the very low Ag content (~0.0053%).

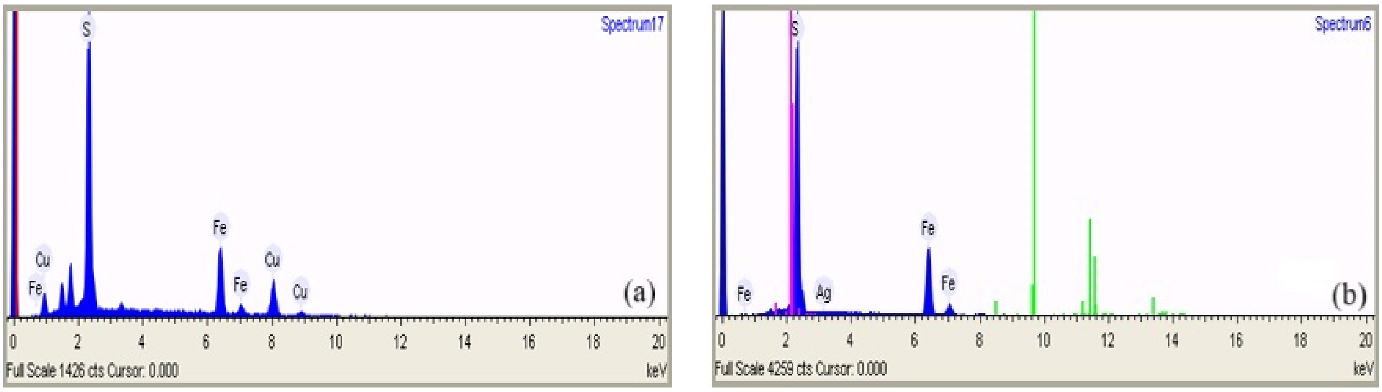

Fig. S3. The SEM-EDS spectra of copper concentrate showing (a) chalcopyrite grains and (b) pyrite grains, with argentite detected at trace levels

TABLE S7

The SEM-EDS results showing elemental weight percentages in the copper concentrate sample

Element	Weight %	
Sulfur	35.5	46.2
Iron	38.1	53.7
Silver	—	0.1
Copper	26.4	—

Figure S3

The SEM-EDS analysis of the concentrate sample revealed the mineral phases present. Fig. 3(a) shows the spectrum corresponding to chalcopyrite grains, while Fig. 3(b) indicates the spectrum of pyrite grains, where argentite was also detected. The detected argentite content was extremely low, approximately 0.1 wt.%.

Information – Bio-oxidation Evidence

Table S8

A progressive decrease in concentrate pH was observed over the 3-month monitoring period, coinciding with increased activity of sulfur oxidizing bacteria and the generation of sulfuric acid (Eqs. (7), (8), (10)) [15,28,29]. These trends are shown in Fig. 3.

An increase in Fe(III) concentration further indicated the activity of iron oxidizing bacteria [15,28,29]. However, only total Fe was measured in this study, as separate determination of Fe(III) and Fe(II) in copper concentrate proved technically challenging.

From the copper concentrate samples 1-N and 2-N, grown on two types of selective bacterial media (TABLES S8 and S9), two distinct acidophilic isolates were obtained: Acidi-40 and Acidi-41. Their initial cultivation and enrichment are shown in Fig. S4.

TABLE S8

Composition of Acidithiobacillus thiooxidans medium-1

No	Compound	Mass	Volume of medium	Sterilization condition
1	KH_2PO_4	0.3 g	Sol A – 95 ml	Autoclave 121°C 15 min
2	$MgSO_4*7H_2O$	0.05 g		
3	$(NH_4)_2SO_4$	0.3 g		
4	$CaCl_2$	0.03 g		
5	$Na_2S_2O_3$	0.5 g	Sol B – 5 ml	filtration

TABLE S9

Composition of Acidithiobacillus medium-2

No	Compound	Mass	Volume of medium	Sterilization condition
1	NH_4Cl	0.01 g	100 ml	Autoclave 121°C 15 min
2	KH_2PO_4	0.3 g		
3	$MgCl_2$	0.01 g		
4	$CaCl_2$	0.01 g		
5	Sulfur	1.0 g		Water bath

Figure S4

Isolation and preliminary observation of acidophilic bacterial colonies from copper concentrate samples (Acidi-1-N and Acidi-2-N). Representative images show (a) sulfur-oxidizing bacterium Acidi-40 and (b) sulfur-oxidizing bacterium Acidi-41 grown on selective media 1 and 2. These results confirm that acidophilic microorganisms capable of thriving under oxidative conditions were successfully enriched from both copper concentrate samples.

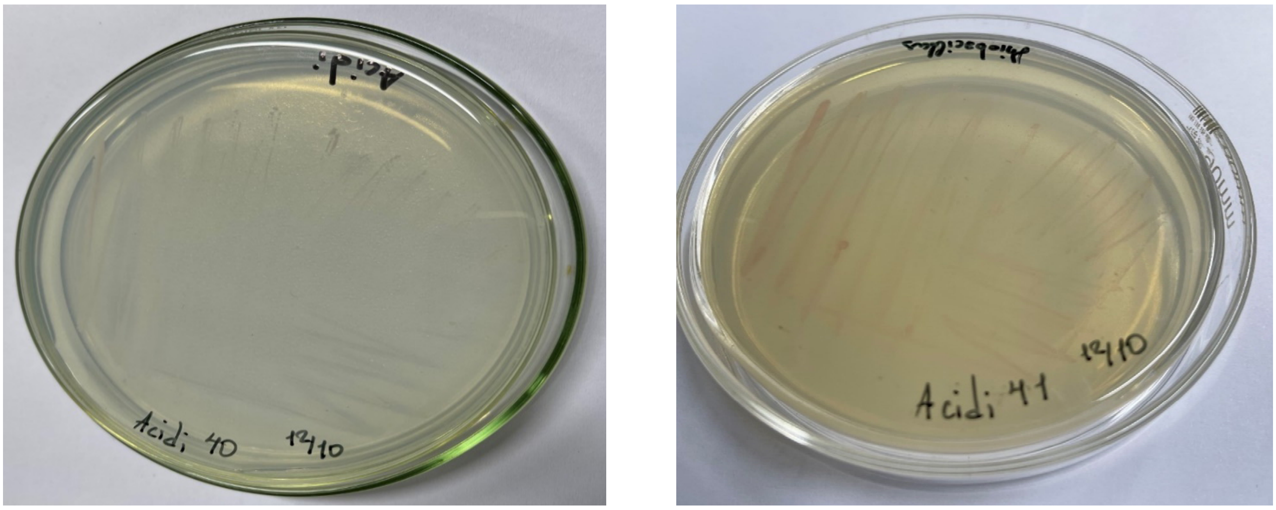

Fig. S4 The column of bacteria (a) sulfur oxidation bacteria Acidi 40 (b) sulfur oxidation bacteria Acidi 41 in the concentrate sample

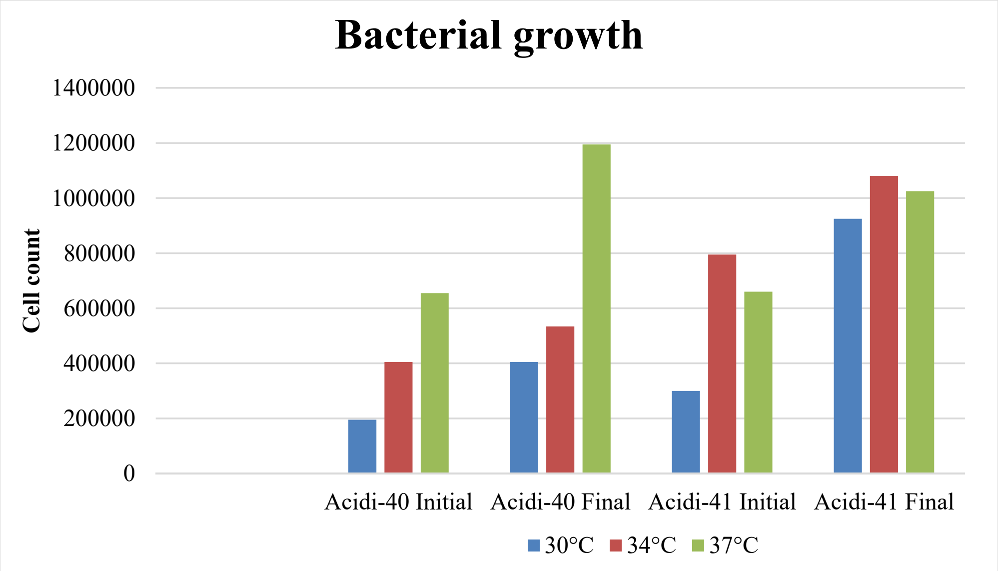

Fig. S5. Bacterial growth of Acidi-40 and Acidi-41 isolates at different temperatures (30°C, 34°C, 37°C)

Figure S5. Growth profiles of Acidi-40 and Acidi-41 isolates at different temperatures (30°C, 34°C, 37°C) over a 7-day incubation period in selective acidic media. Initial and final cell counts demonstrate temperature-dependent growth: Acidi-40 showed the highest multiplication rate at 37°C, while Acidi-41 exhibited stable growth across all tested conditions. These findings confirm the presence of viable sulfur-oxidizing bacteria in the copper concentrate samples, consistent with the bio-oxidation activity observed during Stage II (June-July).